NASA TECHNICAL NOTE

NASA TN D-8148

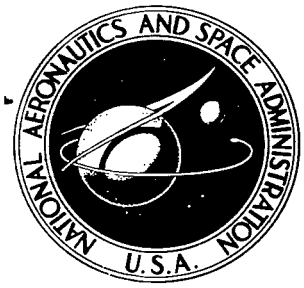

NASA TN D-8148

PREDICTION OF VIKING LANDER CAMERA IMAGE QUALITY

Friedrich O. Huck, Ernest E. Burcher,
Daniel J. Jobson, and Stephen D. Wall

Langley Research Center
Hampton, Va. 23665

NATIONAL AERONAUTICS AND SPACE ADMINISTRATION • WASHINGTON, D. C. • APRIL 1976

1. Report No.	2. Government Accession No.	3. Recipient's Catalog No.
NASA TN D-8148		

4. Title and Subtitle	5. Report Date
PREDICTION OF VIKING LANDER CAMERA IMAGE QUALITY	April 1976
	6. Performing Organization Code

7. Author(s)	8. Performing Organization Report No.
Friedrich O. Huck, Ernest E. Burcher, Daniel J. Jobson, and Stephen D. Wall	L-10626
	10. Work Unit No.
9. Performing Organization Name and Address	815-20-04-03
NASA Langley Research Center Hampton, Va. 23665	11. Contract or Grant No.
	13. Type of Report and Period Covered
12. Sponsoring Agency Name and Address	Technical Note
National Aeronautics and Space Administration Washington, D.C. 20546	14. Sponsoring Agency Code

15. Supplementary Notes

16. Abstract

Formulations are presented that permit prediction of image quality as a function of camera performance, surface radiance properties, and lighting and viewing geometry. Image quality predictions are intended to aid in diagnosing camera performance, in establishing a preflight imaging strategy for the Viking lander mission to Mars, and in rapidly revising this strategy if data returned from Mars reveal unfavorable or unanticipated conditions. Predictions made for a wide range of surface radiance properties reveal that image quality depends strongly on proper camera dynamic range command and on favorable lighting and viewing geometry. Proper camera dynamic range commands depend mostly on the surface albedo that will be encountered. Favorable lighting and viewing geometries depend mostly on lander orientation with respect to the diurnal Sun path over the landing site, and tend to be independent of surface albedo and illumination scattering function. Side lighting with low Sun elevation angles (10^{o} to 30^{o}) is generally favorable for imaging spatial details and slopes, whereas high Sun elevation angles are favorable for measuring spectral reflectances.

17. Key Words (Suggested by Author(s))	18. Distribution Statement
Viking lander camera Image quality	Unclassified – Unlimited Subject Category 35

19. Security Classif. (of this report)	20. Security Classif. (of this page)	21. No. of Pages	22. Price*
Unclassified	Unclassified	76	$4.75

*For sale by the National Technical Information Service, Springfield, Virginia 22161

CONTENTS

PREDICTION OF VIKING LANDER CAMERA IMAGE QUALITY

Friedrich O. Huck, Ernest E. Burcher, Daniel J. Jobson,
and Stephen D. Wall
Langley Research Center

SUMMARY

Formulations are presented that permit predictions of image quality as a function of camera performance, surface radiance properties, and lighting and viewing geometry. Image quality predictions are intended to aid in diagnosing camera performance, in establishing a preflight imaging strategy for the Viking lander mission to Mars, and in revising this strategy if image data returned from Mars reveal unfavorable or unanticipated conditions.

Predictions made for a wide range of surface radiance properties reveal that image quality depends strongly on proper camera dynamic range command and on favorable lighting and viewing geometry. Proper camera commands depend mostly on the surface albedo that will be encountered; to characterize the scene radiance initially, it is better to err with a dynamic range that is too wide to provide a sufficient number of quantized radiance levels for adequate pictures than with a dynamic range that is too narrow to encompass most of the scene radiance. Favorable lighting and viewing geometries depend mostly on the lander orientation with respect to the diurnal Sun path over the landing site, and tend to be independent of surface albedo and illumination scattering function. Side lighting with Sun elevation angles ranging from 10^{o} to 30^{o} is most often favorable for imaging spatial details and slopes. Within this range it is better to err with Sun elevation angles that may prove too high rather than too low for optimum imaging geometry. High Sun elevation angles are always favorable for measuring spectral reflectances.

INTRODUCTION

Two Viking spacecraft, each consisting of an orbiter and a soft lander, are scheduled to arrive at Mars in the summer of 1976 (refs. 1 and 2). Each lander carries two identical facsimile cameras together with many scientific instruments.

The camera (ref. 3) features an array of 12 silicon photodiodes consisting of 4 broadband channels with selectable focus for high-resolution imaging, 1 broadband channel for rapid surveys, 6 narrowband channels for multispectral imaging (color and near-infrared), and 1 narrowband channel for scanning the Sun. The instantaneous fields of view are 0.04^{o}

for the four high-resolution channels and 0.12° for the other channels. The field of view ranges in elevation from 40° above to 60° below the horizon, and in azimuth to 342.5°. High sensitivity is obtained over a wide dynamic range with only 6-bit encoding by the use of 6 commandable linear gains and 32 offsets. The camera scanning rates are synchronized with the lander data transmission rates of 16 000 bits per second to the two orbiters as relay stations and 250 bits per second directly to Earth. Image data can also be stored on a lander tape recorder. About 10^7 bits of image data will be transmitted during most days of the 60-day-long mission planned for each lander.

It is generally known from Lunar Orbiter and Surveyor pictures of the Moon and from Mariner pictures of Mars and Mercury that good image quality depends not only on camera performance but also on lighting and viewing geometry and on surface radiance properties (i.e., albedo and illumination scattering function). Primary concerns for the Viking lander imaging investigation are degradation of camera responsivity by neutron radiation from the lander radioisotope-thermoelectric generators during the year-long cruise to Mars; uncertain lighting and viewing geometry despite efforts to control the lander orientation during final descent; uncertain surface relief and radiance properties; contamination of the camera window by dust adhesion and abrasion from dust storms with velocities up to 70 m/s; delay of several days between receipt of pictures and update of camera commands because of mission constraints; and initial trials and possible errors in selecting suitable camera gains and offsets.

To aid the imaging investigation, this paper presents formulations that permit image quality predictions to be made as a function of camera performance, target radiance properties, and lighting and viewing geometry. Image quality predictions as a function of reference test chart features are intended to aid in diagnosing camera performance. Predictions as a function of surface features are intended to aid in establishing a preflight imaging strategy and in rapidly revising this strategy if image data returned from Mars reveal unfavorable or unanticipated conditions. This paper also presents results of predictions as a function of lighting geometry for a wide range of surface radiance properties to aid in establishing broad guidelines for imaging.

SYMBOLS AND NOTATION

A area, m^2

a_0,a_1,a_2 physical parameters of illumination scattering function (see table V and eq. (48))

$B(u,v,w)$ normalized image contrast of cone section (see eq. (42))

b	number of pixels contained in cone section
c	number of pixels per cone diameter
D	lens diameter, m
e	charge of an electron, C
f	focal length, m
G	channel gain
g	phase angle, deg (see fig. 13)
h	height, m
i_d	photodiode noise-current density, $A/\sqrt{Hz}$
i_e	photosensor-array noise-current density, $A/\sqrt{Hz}$
$J_n( )$	nth order Bessel function
K	photodiode signal current, A
k	Boltzmann constant, J/K
k_c	calibration factor for photosensor-array channels
k_{co}	commandable offset interval, V (see fig. 7)
k_g	gain constant, N_d/V
k_i	ratio of signal integration time to sampling time
k_o	fixed offset, V
L	object distance from lens, m
ℓ	distance from lens in image space, m

N	total rms noise, V
N_d	digital number (see eq. (17))
N_g	gain number (see fig. 7)
N_{off}	offset number (see fig. 7)
N_q	rms quantization noise, V
$N(\lambda;\iota,\epsilon,g)$	object radiance, W/cm^2-sr
NER	noise-equivalent radiance, W/cm^2-sr
$\bar{n}$	surface normal
$o(\chi,\psi)$	normalized spatial object radiance distribution
$R(\lambda)$	spectral responsivity of photosensor array, A/W
R_f	preamplifier feedback resistance, Ω
R_i	channel resistance, Ω
r	radius, m
$S(\lambda)$	solar irradiance, W/cm^2-μm
$S(\chi,\psi)$	camera signal, A
s	dimensionless variable for spatial frequency (see eq. (4))
T	temperature, K
u	dimensionless variable for defocus (see eq. (6))
V	photosensor-array output voltage, V
v	dimensionless aperture radius (see eq. (5))

W	noise-equivalent bandwidth, Hz
w	dimensionless variable for signal integration time (see eq. (11b))
X,Y	camera elevation and azimuth sampling interval, respectively, rad or deg
α	surface or cone slope, deg
β	instantaneous field of view, rad or deg
$\gamma(\lambda)$	mirror reflectance
δ	increment of cone azimuth angle, deg
ϵ	emittance angle, deg (see fig. 13)
ζ	azimuth angle between incident light and cone surface element normal, deg (see fig. 13)
ζ_{sh}	azimuth angle defining cone shadow limits, deg (see fig. 14)
θ	azimuth angle between incident light and camera viewing axis, deg
ι	incidence angle, deg
κ	number of quantization levels
Λ	tribar width on reference test chart, m
λ	wavelength, μm
ν,ω	spatial frequency along elevation and azimuth direction, respectively, lp/rad
$\rho(\lambda)$	albedo
$\tau(\lambda)$	spectral transmittance
$\tau(\chi,\psi)$	point-spread function
$\hat{\tau}(\ )$	spatial frequency response

Υ	optical thickness of atmosphere
$\phi(\iota,\epsilon,g)$	illumination scattering function
$\dot{\chi}$	mirror scan rate, deg/s
ψ	azimuth angle between cone surface normal and camera viewing axis, deg (see fig. 14)
ψ_{sh}	azimuth angle defining limits of visual shadow, deg (see fig. 14)
Ω	angle of numerical aperture, deg (see fig. 8)
$\amalg( )$	sampling or comb function
$\Pi( )$	rectangular function

Subscripts:

a	atmosphere
c	camera
cn	cone
cw	camera contamination window
e	electronic
f	spectral filter
i	image
ℓ	lens
m	Mars
o	flat surface
p	photosensor aperture

pw	photosensor-array window
sh	shadow
v	visible
w	camera window
+	brighter than flat surface
-	darker than flat surface

Abbreviations:

BB	broadband
IR	infrared
lp	line pair
SEA	Sun elevation angle

The symbol Δ in front of a parameter indicates an increment of that parameter.

The bracket $\langle\ \rangle$ around a parameter indicates that parameter which is to be estimated.

A bar over a symbol denotes an average or weighted value.

A circumflex ($\hat{}$) over a symbol denotes a Fourier transform.

CAMERA

Description

Location.- Figure 1 presents a view of the Viking lander. Its two cameras are separated by 0.8 m and view the surrounding terrain from a height of 1.3 m. Figure 2 shows an outline drawing of the field of view available to the cameras. A large segment of the camera field of view is obscured by the lander structure. Important to calibrating the camera performance are three reference test charts, of which each camera can view two. The shaded surface area defines the area accessible to a surface sampler for biological and organic and inorganic chemical analysis.

A roll maneuver (i.e., rotation about an axis parallel to the camera axis) is planned for the final lander descent phase. An important constraint on lander orientation is to avoid shadowing the sampler area at favorable Sun elevations. A general goal is to obtain morning and afternoon lighting of the sampler area, first from one direction and then from the other, to insure that all features in this area can be viewed at one time or another out of shadow. However, contrary to the best efforts of the flight engineers, the spacecraft may land in an orientation that results in a different, less favorable lighting geometry.

Construction.- Figure 3 presents a simplified cutaway view of the camera. The upper elevation assembly rotates in azimuth during operation, and the lower azimuth assembly is bolted to the lander. General design and operating characteristics are listed in table I and performance characteristics in table II.

The thin camera housing and the major support structure are made of beryllium to provide lightness, stiffness, and low thermal expansion and contraction. The inner surfaces of the housing are treated with a matte black finish to reduce internal light reflections, and the outer mating surfaces are gold plated to suppress electromagnetic interference. A 3- to 5-cm-thick blanket of fiberglass and aluminum foil insulates the entire camera to reduce radiative and convective transfer to the cold Martian atmosphere. In addition, thermostatically controlled heaters are located in the vicinity of critical components to maintain their temperature above -40° C.

The elevation assembly is hermetically sealed and filled with argon gas at a pressure of nearly 1 bar (10^5 N/m^2). The azimuth assembly is exposed to the Martian atmosphere. However, dust is prevented from entering by a labyrinth seal between the rotating and stationary parts of the camera.

The camera has two 2.5-mm-thick fused silica windows, each with an outer coating of SiO_2, which discourages dust adhesion and abrasion, and an inner coating of MgF_2, which reduces internal light reflections. The outer window, referred to as the contamination cover and not shown in figure 3, is hinged on one side and spring-loaded. By rotating the camera nearly 360° in a rapid slew mode, a lever can be forced against the side of the dust post with sufficient impact to release a catch on the contamination cover; a spring then moves the cover out of the optical path. This cover protects the inner window from gaseous condensation during the lander heat sterilization process prior to flight, and from dust contamination during the first few days or weeks of operation on Mars.

The narrow window entrance usually hides behind a post to avoid unnecessary exposure to dust. The post contains two small tungsten filament light sources that permit the camera performance to be checked when the lander is stored inside the Viking spacecraft during the flight to Mars. Carbon dioxide carried under pressure in a container inside the lander can be released on command through a tube, which is attached to the post, to blow dust off the window.

Light which passes through the window is reflected by a mirror that nods up and down to provide the elevation scanning; scan profile and rates are given in figure 4. Image data are acquired only during the relatively slow upward motion. The reflected light is imaged by an achromatic triplet lens onto a photosensor array. The lens aperture diameter is 0.95 cm and the focal length is 5.37 cm. Light falling on the photosensor array is transduced into an electrical signal.

Immediately below the lens is a dark reference shutter which consists of a rotary solenoid that controls a paddle-shaped black metal shutter. When the solenoid is energized, the solenoid shaft moves the shutter over the exit pupil of the lens to block external light from the photosensor array. The design includes a spring that forces the shutter to the open position in case of a failure of the solenoid or associated electronics. The dark reference shutter is closed for sampling the photosensor-preamplifier dark current, which is stored for later subtraction from the signal current, and for calibrating the photosensor array with a small tungsten filament lamp located below the shutter. The inner surface of the optical tunnel between the lens and the photosensor array contains a multiaperture baffle that is designed not only to reduce veiling glare but also to attenuate radio-frequency interference from the lander antennas.

The elevation assembly, which contains the camera elements described so far, tapers down to a narrow shaft below the photosensor array. All the cables that provide connections between the electrical elements in the elevation assembly and the control and signal processing electronics in the azimuth assembly spiral down through the inside of this shaft. The azimuth servo assembly, which is mounted on the outside of the shaft, is similar to the elevation servo assembly mounted on the mirror shaft. Both assemblies consist of a torque motor, a tachometer, and a resolver.

Signal flow.- The light-sensitive part of the photosensor array is a miniature array of 12 silicon photodiodes. Their responsivities are plotted in figure 5. Four of the diodes are spaced at different distances from the lens for electrical focus selection for high-resolution (black-and-white) imaging. Six of the other diodes are covered with optical filters for multispectral (color or infrared) imaging. Another diode is unfiltered and used for rapid surveys of the terrain, and one is covered with a red filter and used for viewing the Sun directly. The nominal aperture diameter is 0.041 mm for the high-resolution diodes, and 0.119 mm for the low-resolution diodes.

The cameras are exposed to a steady flow of neutrons and gamma rays from the lander radioisotope-thermoelectric generator during the nearly year-long cruise from Earth to Mars. Radiation damage by the neutrons degrades the photodiode performance, particularly in the infrared region from 0.8 to 1.1 μm, where the absolute responsivity will be reduced by an estimated 15 to 40 percent and the temperature dependence of the relative responsivity will be increased.

Figure 6 shows a simplified circuit diagram of the photosensor array and video processing electronics. Eleven of the diodes have their own preamplifier to convert their small output current into a usable signal, while the Sun diode signal current is sufficiently high to be directly handled by the video processing electronics. The preamplifiers are conventional current-to-voltage converters. Their outputs are summed into a buffer amplifier. The gain of this stage is the ratio of the amplifier feedback resistance to the input resistance of each channel. The input resistances were selected to compensate for different photodiode aperture sizes and filter transmittance characteristics.

The output from the summing amplifier is passed to circuits which provide commandable gains and offsets, automatic dark-current subtraction, and analog-to-digital (A/D) conversion. The primary electrical filtering which the signal undergoes is the integration in the A/D converter.

Six gains can be commanded in steps of powers of 2, and 32 offsets can be commanded in small steps from a slightly negative offset up to nearly the full dynamic range of the camera, as shown in figure 7. These commandable gains and offsets provide a means of decreasing quantization intervals (at the expense of dynamic range) without increasing data bits per pixel.

Control logic.- Camera operation is controlled by a 48-bit command word from the lander guidance, control, and sequencing computer. When the camera logic senses that the lander computer has turned on power for the camera, it clears all its memory elements and commands the azimuth and elevation servos to a preset position. Immediately after, the azimuth start and elevation pointing angles are loaded into their respective counters, forcing the servos to slew to the commanded positions. Upon receipt of clock pulses from the lander data acquisition and processing unit, the camera logic selects first engineering data (such as temperature) from various sources and then video data. Video data from the A/D converter are passed through a 524-bit memory which converts the 75-percent mirror scanning efficiency to a 90-percent video data format efficiency. This process is repeated for each line scan in an image. Three imaging modes can be commanded:

(1) A high-resolution imaging mode is effected by sending one incrementing pulse to the elevation servo between video samples and to the azimuth servo between active line scans.

(2) A low-resolution (survey) imaging mode is effected by tripling the number of incrementing pulses sent to the elevation servo between video samples and to the azimuth servo between active line scans.

(3) A multispectral (color or infrared) imaging mode is effected by alternately selecting three diodes (either blue-green-red-blue, etc. or IR3-IR2-IR1-IR3, etc.) for

successive elevation scans and inhibiting the azimuth servo until three elevation scans have been completed.

In addition, repeated line scans are effected by inhibiting the azimuth servo. This mode is used for radiometric measurements of atmospheric and surface features, and for observing variable features.

Data are acquired at either one of two rates: synchronous with the lander data transmission rate of 16 000 bits per second to one of the two Viking orbiters, or 250 bits per second directly to Earth. Data acquired at either rate can also be stored on a lander tape recorder, permitting the cameras to be used during favorable imaging opportunities independent of data transmission periods. Typical picture formats and their data content are listed in table III.

Analytical Model

Imaging process.- The process by which the facsimile camera transfers the (continuous) object radiance distribution $o(\chi,\psi)$ into a (discrete) electrical signal $S(\chi,\psi)$ can be approximately formulated by the expression (ref. 4)

$$S(\chi,\psi) = K\left[o(\chi,\psi) * \tau_c(\chi,\psi)\right] \amalg\left(\frac{\chi}{X},\frac{\psi}{Y}\right) \tag{1}$$

where K is the photodiode current for uniform radiance; $\tau_c(\chi,\psi)$, the camera point-spread function; χ and ψ, the angular elevation and azimuth imaging coordinates, respectively; and X and Y, the angular elevation and azimuth sampling intervals, respectively. The symbol $*$ denotes convolution, and $\amalg\left(\frac{\chi}{X},\frac{\psi}{Y}\right)$ denotes the sampling (ref. 5) or comb (ref. 6) function. The azimuth sampling interval Y is equal to the camera azimuth stepping interval times $\cos\chi$, where χ is measured from a plane normal to the optical axis of the objective lens.

An approximation is introduced into the formulation of equation (1) by the separation of spatial and spectral object and camera characteristics. Actually, $o(\chi,\psi)$ and $\tau_c(\chi,\psi)$ are functions of wavelength, and the spatial convolution should therefore be integrated over wavelength. However, it is generally convenient to separate spatial and spectral characteristics, and let the average photosensor signal current K account for the spectral characteristics. This approximation permits $o(\chi,\psi)$ and $\tau_c(\chi,\psi)$ to be expressed as normalized functions, whereas $S(\chi,\psi)$ takes on the dimension of K. It requires that all spatial computations be performed at the surface-radiance and camera-responsivity weighted wavelength $\bar{\lambda}$.

The optical-mechanical line-scan imaging process of the facsimile camera is implicitly a function of time. The formulation of equation (1) implies therefore that the convolution of the object radiance distribution with the camera point-spread function be performed as a function of the time each pixel is acquired in a picture (ref. 7). However, if neither object radiance distribution nor camera response varies with time (as is assumed here), then it is immaterial whether the pixels in a picture are formed simultaneously or sequentially.

The imaging process of the facsimile camera is more conveniently evaluated in the frequency rather than spatial domain. The Fourier transform of equation (1) can be written as

$$\hat{S}(\nu,\omega) = K\,\hat{o}(\nu,\omega)\;\hat{\tau}_c(\nu,\omega) * XY\;\Pi(X\nu,Y\omega) \tag{2}$$

where ν and ω are the spatial frequency along the elevation and azimuth direction, respectively, and the circumflexes represent the respective Fourier transform variables of the functions in equation (1). After this signal is passed through a proper low-pass filter,

$$\hat{S}(\nu,\omega) \approx K\,\hat{o}(\nu,\omega)\;\hat{\tau}_c(\nu,\omega) \tag{3}$$

The approximation given by equation (3) disregards all frequency components of the sidebands that may fall into the passband of the filter and cause image degradation due to aliasing. (See refs. 3, 8, and 9 for details.)

Spatial response.- The spatial frequency response of the camera $\hat{\tau}_c$ is the product of the frequency responses of the objective lens $\hat{\tau}_\ell$, photosensor aperture $\hat{\tau}_p$, and signal electronics $\hat{\tau}_e$. To formulate and evaluate the camera frequency response, it is convenient to change from spatial variables (ν and ω) to dimensionless variables (s, v, and u). The latter take advantage of the circular symmetry of the objective lens and photosensor aperture, and allow numerical results of the following equations to be readily used for a variety of specific configurations.

Spatial frequency is accounted for by the dimensionless variable s given by (ref. 10)

$$s = \frac{\bar{\lambda}\left(\nu^2 + \omega^2\right)^{1/2}}{\ell_i \sin \Omega} \approx \frac{2\bar{\lambda}}{D}\left(\nu^2 + \omega^2\right)^{1/2} \tag{4}$$

where $\bar{\lambda}$ is the surface-radiance and camera-responsivity weighted wavelength; ℓ_i, the distance from the image plane to the lens; $\sin \Omega$, the numerical aperture; and D, the

diameter of the objective lens. (See fig. 8.) The photosensor aperture radius r_p and the instantaneous field of view β formed by this aperture are accounted for by the dimensionless variable v given by (ref. 10)

$$v = \frac{2\pi}{\bar{\lambda}} r_p \sin \Omega \approx \frac{2\pi}{\bar{\lambda}}\left(\frac{D}{2\ell_p}\right) r_p \approx \frac{\pi}{\bar{\lambda}}\left(\frac{D}{2}\right)\beta \tag{5}$$

where ℓ_p is the distance between the lens and the aperture. The amount of defocus introduced by differences in image-plane and aperture-plane distances from the lens is accounted for by the dimensionless variable u given by (ref. 10)

$$u = \frac{2\pi}{\bar{\lambda}} \Delta\ell \tan \Omega \sin \Omega \approx \frac{\pi}{2\bar{\lambda}} \Delta\ell \left(\frac{D}{\ell_i}\right)^2 \tag{6}$$

where $\Delta\ell = \left|\ell_i - \ell_p\right|$. Object-space distances L are related to image-space distances ℓ by the thin-lens formula

$$\frac{1}{f} = \frac{1}{L} + \frac{1}{\ell} \tag{7}$$

where f is the lens focal length.

The lens performance is essentially diffraction limited over the angular extent of the photodiode array. The frequency response of a defocused, diffraction-limited lens has been formulated by Hopkins (refs. 11 and 12) as

$$\begin{aligned}\hat{\tau}_\ell(u;s) = \frac{4}{\pi us} \cos\left(\frac{1}{2} us^2\right)\Big\{\gamma J_1(us) + \frac{1}{2}\sin 2\gamma\left[J_1(us) - J_3(us)\right] - \frac{1}{4}\sin 4\gamma\left[J_3(us)\right. \\ \left. - J_5(us)\right] + \cdots\Big\} - \frac{4}{\pi us}\sin\left(\frac{1}{2} us^2\right)\Big\{\sin\gamma\left[J_0(us) - J_2(us)\right] - \frac{1}{3}\sin 3\gamma\left[J_2(us)\right. \\ \left. - J_4(us)\right] + \frac{1}{5}\sin 5\gamma\left[J_4(us) - J_6(us)\right] - \cdots\Big\}\end{aligned} \tag{8a}$$

where $\gamma = \cos^{-1}\frac{s}{2}$. As the photosensor aperture approaches focus (u = 0), the lens response becomes

$$\hat{\tau}_{\ell}(0,s) = \frac{1}{\pi}(2\gamma - \sin 2\gamma) \tag{8b}$$

Table II lists the in-focus object distances L_p for the photodiodes. Numerical results of equations (8) for various amounts of defocus are presented in figure 9(a). If the best-focused high-resolution diode (see table II) is used at each distance, then $u \leqq 15$ for object distances of 1.7 m to infinity; for the low-resolution diodes, $u \leqq 45$.

The photosensor apertures are circular, and their frequency response is given by

$$\hat{\tau}_p(vs) = \frac{2J_1(vs)}{vs} \tag{9}$$

Numerical results of equation (9) are plotted in figure 9(b).

The primary electrical filtering occurs in the running mean integrator of the A/D converter. The frequency response is

$$\hat{\tau}_e = \operatorname{sinc}\left(\dot{\chi} T_i \nu\right) = \operatorname{sinc}\left(k_i X \nu\right) \tag{10}$$

where $\operatorname{sinc} x = \frac{\sin \pi x}{\pi x}$; $\dot{\chi}$, the mirror line-scan rates (given in fig. 4); T_i, the integration time; and k_i (=0.44), the fraction of the sampling interval $X = \beta$ during which the signal is integrated. Substituting equation (4) for ν (with $\omega = 0$) yields

$$\hat{\tau}_e(ws;\omega=0) = \operatorname{sinc} ws \tag{11a}$$

where

$$w = \frac{D}{2\bar{\lambda}} k_i \beta \tag{11b}$$

Numerical results of equations (11) are plotted in figure 9(c).

The spatial frequency response of the camera as a function of the dimensionless variables is

$$\hat{\tau}_c(u,v,w;s) = \hat{\tau}_{\ell}(u,s)\ \hat{\tau}_p(vs)\ \hat{\tau}_e(ws;\omega=0) \tag{12}$$

Numerical results of equation (12) are plotted in figure 9(d).

Spectral response.- The photodiode current $K(\iota,\epsilon,g)$ for a spatially uniform radiance $N(\lambda;\iota,\epsilon,g)$ is predicted by (ref. 10)

$$K(\iota,\epsilon,g) = \left(\frac{\pi}{4}\right)^2 D^2 \beta^2 k_c \int_0^\infty N(\lambda;\iota,\epsilon,g)\ \tau_c(\lambda)\ R(\lambda)\ d\lambda \tag{13}$$

where $\tau_c(\lambda)$ is the optical throughput of the camera, and $R(\lambda)$ and k_c are the responsivity and calibration factor, respectively, of each photosensor-array channel.

The radiance of a surface is

$$N(\lambda;\iota,\epsilon,g) = \frac{1}{\pi} S(\lambda)\ \tau_a\left(\iota_o;\lambda\right)\ \rho(\lambda)\ \phi(\iota,\epsilon,g) \tag{14}$$

where $S(\lambda)$ is the solar irradiance; $\tau_a\left(\iota_o;\lambda\right)$, the atmospheric transmittance; and $\rho(\lambda)$ and $\phi(\iota,\epsilon,g)$, the surface albedo and illumination scattering function, respectively.

The optical throughput of the camera is

$$\tau_c(\lambda) = \begin{cases} \tau_{cw}(\lambda)\ \tau_w(\lambda)\ \gamma(\lambda)\ \tau_\ell(\lambda) & \text{(cover in place)} \\ \tau_w(\lambda)\ \gamma(\lambda)\ \tau_\ell(\lambda) & \text{(cover removed)} \end{cases} \tag{15}$$

where $\tau_{cw}(\lambda)$, $\tau_w(\lambda)$, and $\tau_\ell(\lambda)$ are the transmittance of the contamination cover, window, and lens, respectively, and $\gamma(\lambda)$ is the reflectance of the mirror. Values are plotted in figure 10.

The responsivity for each photosensor-array channel is

$$R(\lambda) = \tau_{pw}(\lambda)\ \tau_f(\lambda)\ R'(\lambda)$$

where $\tau_{pw}(\lambda)$ is the transmittance of the photosensor-array window (about 0.96); $\tau_f(\lambda)$, the spectral filter (if present) transmittance; and $R'(\lambda)$, the photodiode responsivity. Values of $R(\lambda)$ are plotted in figure 5.

The photosensor output voltage $V(\iota,\epsilon,g)$ for a photodiode current $K(\iota,\epsilon,g)$ (see fig. 6) is

$$V(\iota,\epsilon,g) = K(\iota,\epsilon,g)\ R_f G \tag{16}$$

where R_f is the preamplifier feedback resistance and G the channel gain.

The calibration factor k_c for each camera channel is selected so that predicted photosensor-array output voltages V, from equations (13) and (16), agree with camera calibration measurements. Camera response and calibration data are given in appendix A.

The quantized signal, or digital number N_d, is related to an analog signal V by (see fig. 7)

$$N_d = \frac{k_g}{2^{N_g}}\left(V - k_{co}N_{off} + k_o\right) \tag{17}$$

where N_g is the commandable gain number (ranging from 0 to 5); N_{off}, the commandable offset number (ranging from 0 to 31); k_g, the gain constant $\left(\text{in } N_d/V\right)$; k_{co}, the offset interval; and k_o, the fixed offset.

The surface-radiance and camera-responsivity weighted wavelength $\bar{\lambda}$ at which all spatial computations should be performed is given by

$$\bar{\lambda} = \frac{\int_0^\infty \lambda\, S(\lambda)\, \tau_a\left(\iota_o;\lambda\right)\, \rho(\lambda)\, \tau_c(\lambda)\, R(\lambda)\, d\lambda}{\int_0^\infty S(\lambda)\, \tau_a\left(\iota_o;\lambda\right)\, \rho(\lambda)\, \tau_c(\lambda)\, R(\lambda)\, d\lambda} \tag{18}$$

Noise.- The two most significant electronic noise sources in the photosensor array are shot noise in the photodiode current and Johnson noise in the preamplifier feedback resistor. Their equivalent noise-current density $\left(\text{in } A/\sqrt{Hz}\right)$ at the input of the preamplifier is (ref. 3)

$$i_e = \sqrt{2ei_d + \frac{4kT}{R_f}} \tag{19}$$

where e is the charge of an electron; i_d, the photodiode current; k, the Boltzmann constant; and T, the absolute temperature. It is generally complicated to account rigorously for variations in shot noise as a function of variations in the photodiode current; instead, an average value for the shot noise based on the signal current $K = K(\iota=\epsilon=g=0)$ (i.e., for $\phi(\iota,\epsilon,g) = 1$) is used as a conservative approximation. Figure 11 presents a plot of the total photosensor noise-current density i_e as a function of the signal current K.

The quantization of the electrical signal for transmission is a basic limitation of digital data in providing the true value of a signal, just as random noise is a limitation of

analog data. For $\kappa(=64)$ uniformly spaced quantization levels within the dynamic range $\Delta V = \left(\frac{\kappa - 1}{k_g}\right)2^{N_g}$, the effective mean-square quantization noise (ref. 13) is

$$N_q^2 = \frac{\Delta V^2}{12\kappa^2} \approx \frac{2^{2N_g}}{12k_g^2} \tag{20}$$

When electronic noise and quantization noise are combined, the total rms noise magnitude referred to the photosensor-array output becomes

$$N = \sqrt{\left(i_e R_f G\right)^2 W + N_q^2} \tag{21}$$

where W is the noise-equivalent bandwidth of the video processing electronics ($W = 2.8$ kHz for the rapid scan rate and $W = 55$ Hz for the slow scan rate).

Sensitivity.- A common measure of sensitivity is the signal-to-rms-noise ratio V/N, where V is the photosensor-array signal voltage given by equation (16) for $\phi(\iota,\epsilon,g) = 1$, and N is the rms noise given by equation (21). A related performance parameter is the noise-equivalent radiance NER given by

$$NER = \frac{N}{V}\int_0^\infty N(\lambda)\, d\lambda \tag{22}$$

where $N(\lambda)$ is given by equation (14). Typical values are given in table IV.

Diagnosis

If the quality of the initial pictures received from the lander is adequate and roughly concurs with preflight predictions, then the basic preflight imaging strategy can be continued with only minor changes to optimize camera commands for subsequent investigations and to respond to terrain features of special interest. However, if the quality of the pictures is poor, then the preflight imaging strategy may need to be revised. Poor image quality could arise because of unanticipated surface properties, unfavorable lander orientation, or degraded camera performance.

A computer program for image quality prediction should aid first as a diagnostic tool in isolating the cause of picture degradation, and thereafter as a predictive tool in revising the imaging strategy. This diagnostic and predictive function can be accomplished as follows: If image data of a reference test chart agree with predictions, then the camera must be operating properly and the poor quality of pictures of the terrain

must have been caused by unanticipated surface radiance properties. However, if image data of a reference test chart disagree with predictions, then the poor quality of all pictures will probably have been caused, at least in part, by a degradation in camera performance. Whatever the initial pictures and camera engineering data may reveal, the resultant conjectures about degraded camera performance and unanticipated scene radiance properties can be accounted for with a prediction computer program by altering pertinent camera and scene parameters until predictions come into agreement with the image data. Thereafter, the prediction program can again aid in establishing favorable camera commands and lighting and viewing geometries.

To accomplish the diagnostic function, it is necessary to predict camera performance in terms of reference test chart features. Three identical reference test charts are located on top of the lander for this reason. Each camera can view two of these charts at a distance of about 1 m. A reference test chart is shown in figure 12; it provides 11 reflectance references (gray patches) for radiometric calibrations, 3 color patches to aid reconstruction of color images, and 3 tribars to check the camera frequency response.

The reflectances of the gray and color patches are nearly Lambertian for light incidence angles ranging from 20^{o} to 60^{o}; the reflectances of the gray patches are also nearly constant, within ±5 percent, with wavelength from 0.4 to 1.0 μm. The absolute reflectances given in figure 12 can be used with these simplifications with a 2-sigma accuracy of ±9 percent. Absolute radiometric camera performance predictions may be checked by substituting $\cos \iota$ for $\phi(\iota,\epsilon,g)$ and absolute reflectance values for $\rho(\lambda)$ in the surface radiance equation (14), and corrected by changing camera parameters until predictions and camera data agree. Camera parameters which may typically be adjusted are the window transmittance $\tau_W(\lambda)$ or the photosensor-array calibration constants k_c.

The reflectances of the gray patches relative to each other are accurate to within ±4 percent for any incidence angle and wavelength. This higher accuracy is important because the ratio of reflectances will noticeably change with appreciable dust adhesion or abrasion and will thus give warning to be careful about the use of the reference test chart as an absolute reflectance reference.

The three tribars of the reference test chart provide an aid in checking the camera frequency response. The camera signal is predicted as a function of its (one-dimensional) sine-wave frequency response $\hat{\tau}_c(\nu)$ along the elevation line-scan direction by the expression

$$\Delta V = \frac{4}{\pi} V(\iota) \left[\sum_{\substack{i=1 \\ j=2i-1}}^{3} \frac{(-1)^{i+1}}{j} \hat{\tau}_c(u,v,w;js) \right] \operatorname{sinc} \frac{\beta L}{57.3\Lambda} \tag{23}$$

Sufficient accuracy is obtained with the first three terms of the expansion. The sampling process generates a signal which is statistical rather than deterministic in nature. The factor $\text{sinc}\,\frac{\beta L}{57.3\Lambda}$ accounts for an average reduction in signal contrast; the actual signal may have a slightly higher or lower contrast. The tribar widths Λ are 12.8, 6.5, and 4.4 mm per line pair (corresponding at 1 m to 1.4, 2.7, and 3.9 lp/deg, respectively). Appendix B presents a comparison of predicted camera square-wave responses with measurements.

IMAGE QUALITY CRITERIA

Definition

A single criterion cannot completely describe the quality of an image; the most that one can hope to do is to define a criterion that is satisfactory for a particular objective. The objective of this study is to optimize lighting and viewing geometry and camera gains. Within this constraint it can be said that it is desirable to resolve small spatial details and slope variations in the broadband (survey and high-resolution) imaging modes, and subtle spectral reflectance variations in the narrowband (color and IR) imaging modes.

The capability to resolve small spatial details and slopes is defined here as the minimum detectable cone diameter and cone slope with respect to a level surface. An upright cone with surface properties of the surrounding terrain seems intuitively representative of many features and has no preferred surface orientation azimuthally about its axis. If the cone angle is chosen to be steep, a condition yielding high surface contrast, then the detectability of this target becomes primarily a measure of the camera capability to resolve small detail. If the cone angle is chosen to be shallow, a condition yielding low surface contrast, then the detectability of the same target becomes primarily a measure of the camera capability to resolve shallow slopes. Cones have previously been used for image quality predictions for the Ranger (ref. 14) and Lunar Orbiter (ref. 15) missions.

The capability to resolve surface reflectance variations in each one of the camera spectral channels is defined as minimum detectable albedo difference, that is, that difference in albedo which results in a given signal-to-noise ratio, a level surface being assumed.

Formulation

Lighting and viewing geometry.- Figure 13 defines the angular relationships between surface slopes and lighting and viewing geometry. The illumination scattering function $\phi(\iota,\epsilon,g)$ accounts for the dependence of surface reflectance on this geometry as a function of the angle ι between incident radiation and surface normal, the angle ϵ between

emitted radiation and surface normal, and the phase angle g between incident and emitted radiation. These three angles can be determined from the following relationships:

$$\cos g = \cos \epsilon_o \cos \iota_o + \sin \epsilon_o \sin \iota_o \cos \theta \tag{24}$$

$$\cos \iota = \cos \alpha \cos \iota_o - \sin \alpha \sin \iota_o \cos \zeta \tag{25}$$

$$\cos \epsilon = \cos \alpha \cos \epsilon_o - \sin \alpha \sin \epsilon_o \cos \psi \tag{26}$$

where ϵ_o and ι_o are the emittance and incidence angles, respectively, for a level surface $\left(\text{with normal } \bar{n}_o\right)$, α is the angle of a surface element with respect to a level surface (and with normal $\bar{n}$), θ is the azimuth angle between incident radiation and the camera optical axis, and ζ and ψ are azimuth angles of the plane formed by the normals $\bar{n}$ and $\bar{n}_o$ with respect to incident radiation and the camera, respectively. The three azimuth angles are related by

$$\theta + \zeta + \psi = 2\pi \tag{27}$$

Cone geometry.- This formulation generally follows the geometric relationships derived by Rindfleisch and Willingham (ref. 14). However, their relationships were constrained to nearly vertical viewing geometries so that no part of the cone, including its shadow (if present), could be obscured from the camera view by the cone itself. This constraint is not valid for a camera viewing a scene from a lander. Relationships from reference 14 are therefore generalized to account for those viewing geometries in which part of the cone or its shadow is obscured from the camera view by the cone itself.

Figure 14 illustrates the geometry of an upright cone with a base of radius r_{cn}, a height h_{cn}, and a slope α defined so that

$$\alpha = \tan^{-1} \frac{h_{cn}}{r_{cn}} \qquad \left(0 < \alpha < \frac{\pi}{2}\right) \tag{28}$$

A surface element with normal $\bar{n}$ is given in terms of the azimuth angle increment δ as

$$\Delta A = \frac{\delta r_{cn}^2}{2 \cos \alpha} \tag{29}$$

If $\iota_o \geqq 90^o - \alpha$, a shadow is cast by the cone on a level surface (as shown shaded in fig. 14(a)) for $-\zeta_{sh} < \zeta < \zeta_{sh}$, where $\zeta_{sh} = \cos^{-1} \frac{1}{\tan \alpha \tan \iota_o}$; this shadow has an area

$$A_{sh} = r_{cn}^2\left(\tan \zeta_{sh} - \zeta_{sh}\right) \tag{30a}$$

Similarly, if $\epsilon_o \geqq 90^o - \alpha$, a "visual" shadow is formed (fig. 14(b)) which obscures part of the cone and possibly part of the cone shadow (if there is one) from the camera. It is assumed that the rays of light intercepted by the camera are parallel instead of convergent, since only small targets are of interest and the convergence angle is therefore small. Under this condition, area elements ΔA of the cone not visible to the camera are defined by the range $-\psi_{sh} < \psi < \psi_{sh}$, where $\psi_{sh} = \cos^{-1} \frac{1}{\tan \alpha \tan \epsilon_o}$. The shadow area still visible to the camera becomes (see fig. 14(c))

$$A_{v,sh} = r_{cn}^2\left(\tan \zeta_{sh} - \zeta_{sh} - \tan \xi + \xi\right) \tag{30b}$$

where $\xi = \frac{1}{2}\left(\zeta_{sh} + \psi_{sh} - \theta\right)$.

Several geometries must be accounted for when equation (30b) is used. The azimuth angle θ between incident radiation and the camera optical axis must always be chosen so that $\theta < \pi$. When $\theta \geqq \zeta_{sh} + \psi_{sh}$, the "visual" shadow does not overlap any part of the illumination shadow, and equation (30b) reduces to equation (30a). When $\theta + \zeta_{sh} \leqq \psi_{sh}$, the illumination shadow is completely contained within the visual shadow, and the angle ξ must be set equal to ζ_{sh} so that $A_{sh} = 0$. When $\theta + \psi_{sh} \geqq \zeta_{sh}$, the visual shadow is completely contained within the illumination shadow, and the angle ξ must be set equal to ψ_{sh}.

Target and background are considered to be of the same material, so that the variation in cone reflectance with azimuth angle is dependent only on the illumination scattering function. But it would still be exceedingly difficult to translate this reflectance variation exactly into an image signal. The reflectance variation is therefore approximated by an average reflectance of that part of the cone which has a higher-than-background reflectance and another part which has a lower-than-background (including shadow) reflectance.

The total projected area of all cone sections which have a higher-than-background reflectance and are visible to the camera may be expressed as

$$A_+ = \Delta A \sum_i \cos \epsilon_i = \frac{r_{cn}^2 \delta}{2 \cos \alpha} \sum_i \cos \epsilon_i \qquad \left(\phi_i(\iota,\epsilon,g) > \phi_o\right) \tag{31}$$

where $\phi_o \equiv \phi\left(\iota_o,\epsilon_o,g\right)$. The average value of the illumination scattering function of this area becomes

$$\phi_+ = \frac{\Delta A}{A_+} \sum_i \phi_i(\iota,\epsilon,g) \cos \epsilon_i = \frac{\sum_i \phi_i(\iota,\epsilon,g) \cos \epsilon_i}{\sum_i \cos \epsilon_i} \qquad \left(\phi_i(\iota,\epsilon,g) > \phi_o\right) \tag{32}$$

Similarly, the total projected area of all cone sections, including the shadow cast by the cone on a level surface (if present), which have a lower-than-background reflectance and are visible to the camera may be expressed as

$$A_- = \Delta A \sum_i \cos \epsilon_i + A_{sh} \cos \epsilon_o = r_{cn}^2 \left[\frac{\delta}{2 \cos \alpha} \left(\sum_i \cos \epsilon_i \right) + \left(\tan \zeta_{sh} - \zeta_{sh} - \tan \xi + \xi \right) \cos \epsilon_o \right]$$

$$\left(\phi_i(\iota,\epsilon,g) < \phi_o\right) \tag{33}$$

The average value of the illumination scattering function of this area becomes

$$\phi_- = \frac{\Delta A}{A_-} \sum_i \phi_i(\iota,\epsilon,g) \cos \epsilon_i = \frac{\delta \sum_i \phi_i(\iota,\epsilon,g) \cos \epsilon_i}{\delta \left(\sum_i \cos \epsilon_i \right) + 2 \cos \alpha \cos \epsilon_o \left(\tan \zeta_{sh} - \zeta_{sh} - \tan \xi + \xi \right)}$$

$$\left(\phi_i(\iota,\epsilon,g) < \phi_o\right) \tag{34}$$

Reflectance inside the shadow is assumed to be negligible.

Cone signal.- Several definitions and assumptions are made to simplify formulations:

(1) According to equation (14), the maximum surface radiance for a given albedo (i.e., for $\phi(\iota,\epsilon,g) = 1$) can be defined as

$$N(\lambda) = \frac{1}{\pi} S(\lambda)\ \tau_a(\lambda)\ \rho(\lambda) \tag{35}$$

The corresponding maximum photosensor signal current and photosensor-array output voltage are defined, respectively, as K and V.

(2) The radiance variation of the cone surface can then be defined as

$$\Delta N_\pm(\lambda) = N(\lambda)\ \Delta\phi_\pm \tag{36}$$

and the corresponding variation in photosensor-array output voltage as

$$\Delta V_{\pm} = V\,\Delta\phi_{\pm} = KRG\,\Delta\phi_{\pm} \tag{37}$$

(3) The two cone areas A_+ and A_- are assumed to be circular in shape with radius r_+ and r_-, respectively; that is, $A_{\pm} = \pi r_{\pm}^2$. Computational requirements are thus reduced, since circular symmetry permits the use of the one-dimensional Hankel transform instead of the general two-dimensional Fourier transform. This assumption is justifiable because most of the radiance contained in the spatial frequency distribution of the cone radiance is generally clustered around the lower spatial frequencies. The assumption is also consistent with the earlier approximation of cone radiance variations by two average values.

(4) The cone radius is expressed in terms of the camera instantaneous field of view β so that $r_{cn} = \frac{c}{2}\beta L$, where L is the distance from target to camera. The product βL is the diameter of a pixel, and c is the number of pixels per cone diameter. The diameters $b_{\pm}$ of the areas $A_{\pm}$ can thus be expressed as a function of pixels as

$$b_{\pm} = \frac{2r_{\pm}}{\beta L} = \frac{cr_{\pm}}{r_{cn}} = c\,\frac{A_{\pm}}{\pi r_{cn}^2} \tag{38}$$

where the areas $A_{\pm}$ are given by equations (31) and (33).

From these definitions and assumptions, the spatial frequency distribution of the cone radiance (in image space) is given by the Hankel transform of the two areas $A_{\pm}$, assumed to be circular with radius $b_{\pm}v$, as

$$\Delta N\left(\lambda;b_{\pm}vs\right) = \Delta N_{\pm}(\lambda)\,\frac{2\pi\int_0^{b_{\pm}v} J_0(v's)\,v'\,dv'}{\int_0^{2\pi}\int_0^{b_{\pm}v} v'\,dv'\,dw} = \Delta N_{\pm}(\lambda)\,\frac{2J_1\left(b_{\pm}vs\right)}{b_{\pm}vs} \tag{39}$$

where s and v are given by equations (4) and (5), respectively.

The effect of the camera frequency response in reducing the contrast of spatial detail is accounted for by the inverse Hankel transform of the product of the cone radiance frequency distribution $\Delta N\left(\lambda;b_{\pm}vs\right)$ and the camera frequency response $\hat{\tau}_c(u,v,w;s)$, as given by

$$\Delta V_{\pm}\left(u,v,w;b_{\pm}\right) = \Delta V_{\pm} \int_0^{\infty} \frac{2J_1\left(b_{\pm}vs\right)}{b_{\pm}vs}\, \hat{\tau}_c(u,v,w;s)\, J_0(vs)\, s\, ds \tag{40}$$

Upon averaging, as a final approximation, over the circular image area of radius $b_{\pm}v$, equation (40) becomes

$$\Delta V_{\pm}\left(u,v,w;b_{\pm}\right) = \Delta V_{\pm} \int_0^{b_{\pm}v} \int_0^{\infty} \frac{2J_1\left(b_{\pm}vs\right)}{b_{\pm}vs}\, J_0(v's)\, s\, ds\, v'\, dv' \tag{41a}$$

Equation (41a) can be rewritten (ref. 16) as

$$\Delta V_{\pm}\left(u,v,w;b_{\pm}\right) = \Delta V_{\pm}\, \Pi\left(\frac{v'}{2b_{\pm}v}\right) B(u,v,w) \tag{41b}$$

where

$$\Pi\left(\frac{v'}{2b_{\pm}v}\right) = \begin{cases} 1 & \left(\left|v'\right| \leq b_{\pm}v\right) \\ 0 & \left(\left|v'\right| > b_{\pm}v\right) \end{cases}$$

and

$$B_{\pm}(u,v,w) = \frac{b_{\pm}^2 v^2}{2} \int_0^{\infty} \left[\frac{2J_1\left(b_{\pm}vs\right)}{b_{\pm}vs}\right]^2 \hat{\tau}_c(u,v,w;s)\, s\, ds \tag{42}$$

Minimum detectable cone diameter and slope.- The detectability of a cone depends on its image contrast and size and on noise. The contrast is given by the foregoing results as

$$\Delta V_{\pm}(u,v,w) = \Delta V_{\pm}\, B(u,v,w) = V\, \Delta\phi_{\pm}\, B(u,v,w) \tag{43}$$

The size is given by two circular areas with radii $b_{\pm}v$. According to the central-limit theorem, the mean of a sample of size n has a standard deviation $\sigma/\sqrt{n}$ if σ is the population deviation. Here σ is the total rms camera noise N given by equation (21), and the number of independent samples n is the ratio of image area to pixel area; that is,

$$n_{\pm} = \pi b_{\pm}^2 \frac{v^2}{\pi v^2} = b_{\pm}^2 \tag{44}$$

The effects of contrast, size, and noise on the detectability of a cone can be combined in an expression for signal-to-noise ratio as

$$\left\langle \frac{S}{N} \right\rangle = \frac{1}{N}\left[\Delta V_+(u,v,w)\ b_+ + \Delta V_-(u,v,w)\ b_-\right] \tag{45a}$$

$$\left\langle \frac{S}{N} \right\rangle = \frac{V}{N}\left[\Delta\phi_+ b_+\ B_+(u,v,w) + \Delta\phi_- b_-\ B_-(u,v,w)\right] \tag{45b}$$

If it is desirable to determine the minimum detectable cone slope, the procedure should be to specify c and then to find the slope α which yields a given value of $\langle S/N \rangle$. Or if it is desirable to determine the minimum detectable cone diameter, the procedure should be to specify α and then find the normalized cone diameter c (in pixels) which yields a given value of $\langle S/N \rangle$. Both procedures require iterative evaluations of equations (45) until a solution with desired accuracy is found. The signal-to-noise ratio $\langle S/N \rangle$ is somewhat arbitrarily taken to be 10.

Minimum detectable albedo difference.- Three assumptions are made: (1) The surface is assumed to be level so that $\phi(\iota,\epsilon,g) = \phi\left(\iota_o,\epsilon_o,g\right)$; (2) the surface albedo is assumed to be constant over the narrow wavelength range of the camera spectral filters; and (3) an albedo difference can be detected for a signal-to-noise ratio V/N somewhat arbitrarily taken to be 3. Hence, if the ratio of photosensor output voltage (eq. (16)) to noise (eq. (21)) is set equal to 3 and solved for $\rho(\lambda)$, the minimum detectable albedo difference becomes

$$\langle \Delta\rho \rangle = \frac{3N}{\frac{\pi}{16}\beta^2 D^2 k_c R_f G\ \phi\left(\iota_o,\epsilon_o,g\right) \int_0^\infty S(\lambda)\ \tau_a\left(\iota_o;\lambda\right)\ \tau_c(\lambda)\ R(\lambda)\ d\lambda} \tag{46}$$

MARS RADIANCE PROPERTIES

Spectral Radiance

The distance of Mars from the Sun varies from a maximum of 1.64 AU at the beginning of the mission to a minimum of 1.46 AU at the end of the mission (ref. 17). The solar irradiance at a distance of 1.6 AU is plotted in figure 15(a).

The atmosphere is considered to be a nonabsorbing "Rayleigh" atmosphere with normal optical thickness $\Upsilon(\lambda)$ plotted in figure 15(b) (ref. 17). The atmospheric transmittance is related to the optical thickness by

$$\tau_a(\iota_o;\lambda) = \exp\left\{-\Upsilon(\lambda)\frac{r_m}{h_a}\left[\sqrt{\left(\frac{r_m + h_a}{r_m}\right)^2 - \sin^2 \iota_o} - \cos \iota_o\right]\right\} \tag{47}$$

where r_m is the planet radius and h_a the equivalent atmospheric height of uniform optical thickness; the Mars radius r_m is 3400 km, and the equivalent atmospheric height h_a is 25 km (ref. 18). Values of $\tau_a(\iota_o;\lambda)$ are plotted in figure 15(c) for several solar incidence angles ι_o.

Figure 15(d) presents plots of normal albedos $\rho(\lambda)$ that are representative for various areas on Mars (ref. 17). Perhaps still higher albedos should be anticipated in the blue-green wavelength range, since, according to a recent report (ref. 19), Martian color data obtained by the U.S.S.R. Mars 4 and 5 spacecraft indicate blue mountains and bluish-green craters.

Illumination Scattering Function

An illumination scattering function formulated by Meador and Weaver (ref. 20) is used here to describe the diffuse reflectance of surfaces as a function of light incidence, emittance, and phase angles. The Meador-Weaver formulation is also a function of three parameters which are intended to represent physical surface properties (particle size, single-particle albedo, and compactness). However, no such significance is attached here to these parameters. They are used only as a convenient means of curve-fitting several illumination scattering characteristics with a single analytical function. Any dependence that the illumination scattering function can be expected to have on wavelength because of diffraction effects is not considered.

The illumination scattering function is given by the expression

$$\phi(\iota,\epsilon,g) = \frac{\cos \iota}{(1 + a_0 + a_1)(\cos \iota + \cos \epsilon)}\left[(1 + a_0 \cos g)\, f(\iota,\epsilon,g;a_2) + a_1(\cos \iota + \cos \epsilon)\right] \tag{48}$$

where $f(\iota,\epsilon,g;a_2)$ is a shadowing correction factor given by

$$f(\iota,\epsilon,g;a_2) = e^{\mu-\nu} + \nu \int_0^1 \exp\left\{\mu - \frac{\nu}{6\pi}\left[3\pi x + 2\left(2 + x^2\right)\left(1 - x^2\right)^{1/2} + 6x \sin^{-1} x\right]\right\} dx$$

Results from this function should be used only for values $f(\iota,\epsilon,g;a_2) \geqq 1$; all other values should be replaced by $f(\iota,\epsilon,g;a_2) = 1$. The parameters μ and ν are given by

$$\mu = \frac{4a_2(1 + \cos g)}{3 \sin g}$$

$$\nu = \frac{\pi a_2(\cos \iota + \cos \epsilon)}{\sin g \cos \iota \cos \epsilon}\left[\sin^2 g + 2(1 + \cos g) \cos \iota \cos \epsilon\right]^{1/2}$$

The latest and apparently best data on the illumination scattering characteristics of Mars are given by Thorpe (ref. 21) from Mariner 9 observations. Comparisons of these data with the Meador-Weaver function led to $a_0 = 0.55$, $a_1 = 0.60$, and $a_2 = 0.18$ (ref. 22); with these values the Meador-Weaver function predicts scattering very close to that given by Thorpe. Consequently, this set of parameters will serve here as nominal values. Three other sets of parameters are considered, as summarized in table V, providing scattering characteristics that range from strong backscatter to near-Lambertian reflectance.

Figures 16 to 18 present plots of the illumination scattering function for a wide range of lighting geometries. Figure 16 presents variations of the Mars (Thorpe) illumination scattering characteristics with incidence angle ι_o for several emittance angles: $\epsilon_o = 40^o$, 50^o, 60^o, and 70^o. The corresponding camera elevation angles are -50^o, -40^o, -30^o, and -20^o, respectively. As illustrated in figure 2, these elevation angles encompass the surface sampler area. Figures 17 and 18 present variations of illumination scattering of the four different surfaces with incidence angle ι_o and azimuth angle θ (see fig. 13), respectively. The emission angle ϵ_o is 60^o, corresponding to a camera elevation angle of -30^o, which points near the center of the sampler area.

IMAGE QUALITY PREDICTIONS

Constraints

Predictions are presented to illustrate variations of image quality with lighting geometry for a wide range of surface radiance properties. The lander orientation with respect to the diurnal Sun path over the landing site imposes important constraints on

lighting and viewing geometries that are not accounted for by the predictions. Thus, otherwise favorable geometries may have to be avoided because of obscuration either by the lander structure or its shadow.

The following constraints minimize the number of predictions necessary to cover a wide range of conditions:

(1) The camera viewing geometry is constrained to an emittance angle ϵ_o of 60^o, or camera elevation angle of -30^o, which points near the center of the sampler area (see fig. 2).

(2) The selection of camera gains is constrained to those dynamic ranges that encompass the assumed surface radiance ranges. Table VI lists the maximum photosensor-array output voltages V for the four albedos shown in figure 15(d).

(3) Broadband image quality predictions are presented as a function of the ratio V/N. Table VII presents these ratios for those combinations of surface albedos and camera gains that encompass the corresponding maximum signal levels. The value V/N = 50 is regarded to represent low signal-to-noise ratios; V/N = 100, average signal-to-noise ratios; and V/N = 200, high signal-to-noise ratios.

(4) Cone diameters are expressed as a function of number of pixels c so that predictions can be presented independently of object distance and instantaneous field of view. This simplification is only approximately valid. Defocus blur, for example, is a function of object distance. Also, the lens frequency response affects the smaller spatial detail associated with the narrow instantaneous field of view ($\beta = 0.04^o$) more than the larger spatial detail associated with the broad instantaneous field of view ($\beta = 0.12^o$).

(5) Predictions of cone signal-to-noise ratio $\langle S/N \rangle$ are constrained to cone diameters of 6 pixels and cone slopes of 10^o, 30^o, and 60^o. Predictions of minimum detectable cone slopes $\langle \alpha \rangle$ are constrained to cone diameters of 6 pixels. Predictions of minimum detectable cone diameters $\langle c \rangle$ are constrained to cone slopes of 30^o.

Broadband Image Quality

Table VIII summarizes the broadband image quality predictions that are presented. Appendix C compares some of these predictions with experimental results.

Figures 19 and 20 present graphs of the variation of cone signal-to-noise ratio $\langle S/N \rangle$, minimum detectable cone diameter $\langle c \rangle$, and minimum detectable cone slope $\langle \alpha \rangle$ for the Mars (Thorpe) illumination scattering characteristics. Figure 19 presents these variations as a function of light incidence angle ι_o for three azimuth angles ($\theta = 0^o$, 90^o, and 180^o). Figure 20 presents contour plots of $\langle S/N \rangle$, $\langle c \rangle$, and $\langle \alpha \rangle$ as a function of incidence and azimuth angles.

Results show that the three broadband image quality criteria lead to generally similar conclusions with regard to favorable and unfavorable lighting geometry. However, figure 19 shows that $\langle S/N \rangle$ tends to stress favorable lighting near low Sun elevations, whereas both $\langle c \rangle$ and $\langle \alpha \rangle$ tend to stress unfavorable lighting near small phase angles (i.e., when the Sun is behind the camera, or $\theta = 0^{o}$).

Figures 21, 22, and 23 present graphs of the variation of cone signal-to-noise ratio $\langle S/N \rangle$ with lighting geometry for four illumination scattering characteristics. These variations are presented in figure 21 as a function of incidence angle ι_o for three azimuth angles ($\theta = 0^{o}$, 90^{o}, and 180^{o}) and in figure 22 as a function of azimuth angle θ for three incidence angles $\left(\iota_o = 40^{o}, 60^{o}, \text{and } 80^{o}\right)$. Contour plots of $\langle S/N \rangle$ as a function of incidence and azimuth angles are presented in figure 23.

Results suggest the following conclusions about image quality and lighting geometry:

(1) Image quality depends strongly on the selection of a proper gain (i.e., dynamic range) for a given surface albedo. The dynamic range could be too low to encompass the scene radiance or too high to encode the scene radiance with an adequate number of quantization levels. Initial trials must be made and possible errors in selecting suitable gains must be anticipated.

(2) Image quality depends strongly on lighting geometry. Sun elevation angles ranging from 10^{o} to 30^{o} are most often favorable. Lower Sun elevation angles, ranging from 5^{o} to 20^{o}, tend to be more favorable for detecting shallow slopes, whereas higher Sun elevation angles, ranging from 20^{o} to 40^{o}, tend to be more favorable for imaging steep slopes and large details, such as rocks. Image quality diminishes more rapidly toward elevation angles lower than the most favorable ones rather than toward higher angles. It follows that it is better to err with Sun elevation angles that may prove higher than most favorable rather than lower. Shadows are then also less likely to obscure surface features. Important exceptions exist if the Sun is either behind the camera (i.e., $\theta \approx 0^{o}$) or in front of it (i.e., $\theta \approx 180^{o}$).

If the Sun is behind the camera, then image quality can drastically diminish at small phase angles. Also important, although not a result of the predictions, is that Sun elevation angles below the zero phase angle cause the target to be shadowed by the camera (and lander) structure.

If the Sun is in front of the camera, then favorable Sun elevation angles are dependent on the target, low Sun elevation angles being preferable for cones with low slopes and high Sun angles for cones with steep slopes. It is also important to note, although not revealed by the curves, that the part of the target that faces the camera tends to be in shadow. It follows therefore that side lighting ($40^{o} \lessapprox \theta \lessapprox 120^{o}$) is favorable.

(3) Favorable lighting geometries are independent of surface albedo and do not vary appreciably for illumination scattering characteristics ranging from near-Lambertian reflectances to strong backscatter. However, surfaces with near-Lambertian reflectances provide a wider range of adequate lighting geometries than surfaces with strong backscatter.

Narrowband Image Quality

The variation of minimum detectable albedo difference $\langle \Delta\rho \rangle$ with lighting geometry is essentially dependent only on the surface illumination scattering function. The additional dependence of this variation on atmospheric transmittance is small for Sun elevation angles above 10^{o}. Consequently, plots of the illumination scattering function presented in figures 16 to 18 already reveal much about favorable lighting geometries. More complete information is presented in figure 24 by contour plots of $\langle \Delta\rho \rangle$ as a function of Sun azimuth and elevation angles for four illumination scattering characteristics. Numerical results in figure 24 are given for the green narrowband channel and a gain number of 4. This gain provides a dynamic range that encompasses all but the highest albedo shown in figure 15. Since the sensitivity of all narrowband channels is essentially limited by quantization noise for a gain number of 4, the numerical results approximately represent all narrowband channels. Furthermore, these values multiplied by 2 would approximately represent results for a gain number of 5.

The curves show that high Sun elevation angles are always favorable. However, the preference shown for low phase angles as a result of backscatter is not generally valid. The construction of spectral reflectance curves from multispectral data may be adversely affected by nearly specularlike reflectances, and color pictures with very low surface contrast of both spatial and spectral detail may have a bleached appearance.

CONCLUDING REMARKS

Formulations were presented that permit predictions of image quality as a function of camera performance, surface radiance properties, and lighting and viewing geometry. The general objective of broadband (black-and-white) imaging to resolve small spatial details and slopes was formulated as the detectability of a right-circular cone with surface properties of the terrain. The general objective of narrowband (color and near-infrared multispectral) imaging to resolve spectral reflectance features was formulated as the minimum detectable albedo variation. The camera response was also formulated as a function of reference test chart features to aid in diagnosing its performance. A degraded performance is both diagnosed and simulated by changing camera response characteristics until image quality predictions agree with pictures of the reference test chart.

To satisfy primary objectives of the imaging investigation, it is important that the lander be so oriented that it avoids shadowing the sampler area at favorable Sun elevations. A general goal is to obtain lighting of this area from two sides (i.e., morning and afternoon) so that all features can be viewed at one time or another out of shadow. Results of the image quality predictions suggest the following additional guidelines for imaging:

1. Image quality depends strongly on the proper camera gain command for a given surface albedo. Improper gain commands could result in a dynamic range that is either too narrow to encompass the surface radiance or too wide to provide adequate quantization levels.

2. Image quality depends strongly on lighting geometry. Side lighting with Sun elevation angles ranging from 10^{o} to 30^{o} is most often favorable for broadband imaging. Lower Sun elevation angles, ranging from 5^{o} to 20^{o}, tend to be more favorable for detecting shallow slopes, whereas higher Sun elevation angles, ranging from 20^{o} to 40^{o}, tend to be more favorable for imaging steep slopes and large details, such as rocks. High Sun elevation angles are always favorable for narrowband multispectral imaging.

3. Favorable lighting geometries are independent of surface albedo and do not vary appreciably for a wide range of illumination scattering functions. However, surfaces with near-Lambertian reflectances tend to provide a wider range of adequate lighting geometries than surfaces with strong backscatter.

Langley Research Center
National Aeronautics and Space Administration
Hampton, Va. 23665
March 2, 1976

APPENDIX A

RADIOMETRIC RESPONSE

The purpose of this appendix is to present a complete set of data required to predict camera radiometric response and sensitivity, and to describe absolute radiometric camera calibrations. Data are presented here for only one flight camera (serial no. 08); however, the data are also approximately valid for the other flight cameras. A complete set of data for the four flight cameras is given in reference 23 together with their absolute radiometric calibration data.

Table IX presents optical throughput and photosensor-array responsivities; table X gives photosensor-array electrical characteristics. The gain constant of the video processing electronics k_g is 444.321 N_d/V, the offset interval k_{co} is 0.1441 V, and the fixed offset k_o is 0.204 V.

Absolute radiometric calibrations were made by imaging a reference test chart which, in turn, was illuminated by a lamp that had been calibrated by Eppley Laboratory, Inc., the National Bureau of Standards (NBS). A special calibration fixture was used to insure that the lamp-to-chart distance and the lighting and viewing angles remained constant for all measurements. Four major error sources and the errors are as follows:

Lamp irradiance	±3%
Reference test chart reflectances	±6%
Fixture	±3%
Camera gains and offsets	±3%
Root-sum-square error	±8%

The lamp irradiance was calibrated to an accuracy of ±3 percent in the spectral range 0.4 to 1.1 μm (ref. 24).

The reference test chart reflectances were measured relative to magnesium carbonate ($MgCO_3$), for which the absolute reflectance in this spectral range is known with an accuracy of ±3 percent (ref. 25). Errors introduced by not carefully accounting for some of the variations of this reflectance with wavelength and with lighting and viewing geometry, both in measuring the reference test chart reflectances and in using these reflectance data, diminish the accuracy to ±6 percent. To measure and use reference test chart reflectances more accurately would significantly increase calibration complexity. The reflectances ρ_n of the 11 gray patches are given in figure 12. These reflectances represent the average values of measurements of three reference test charts; the measured reflectances varied less than ±3 percent from these average values (ref. 26). These variations between charts are within measurement errors and are neglected.

APPENDIX A

The calibration fixture was calibrated to account for peculiarities of lighting geometry and for internal reflections which occur despite careful baffling. The remaining uncertainty was estimated to be ±3 percent.

The gain and offset constants k_g, k_{co}, and k_o vary independently with gains, offsets, and temperature (-41° to +10° C) by less than ±2 percent around their average value for each camera; the total error is about ±3 percent. One exception exists: The gain constant k_g for a gain number of 0 differs much more from this value; however, this gain was not used to obtain calibration data.

Predictions made by using equations (13), (16), and (17) and calibration measurements agree if the calibration constants k_c listed in table X are used in equation (13). These calibration constants reveal that the measured photosensor-array output voltages are consistently higher than their predicted values. These discrepancies apparently arise from differences between the methods used for calibrating the photosensor array and in calibrating the cameras, and from light reflections internal to the array (ref. 23).

APPENDIX B

SPATIAL RESOLUTION

The purpose of this appendix is to compare predictions and measurements of the image contrast of three tribars located on the reference test charts. The capability to predict image contrast of known spatial detail aids in diagnosing camera performance.

Figure 25 shows three Viking lander camera images of the reference test chart. The images were obtained with the two nearest-focused high-resolution diodes (BB1 and BB2) and the survey diode. The camera was located 1.0 m from the chart and viewed it normally. Figure 26 compares the normalized contrast of these tribar images with the normalized camera square-wave response $\Delta V/V(\iota)$ predicted by equation (23). Predictions and measurements are in good agreement, the larger tribar being distinctly reproduced in all three images. Contrast of the medium tribar is slightly reduced in the BB1 image, significantly reduced in the BB2 image, and reduced to near threshold in the survey image. The smallest tribar is resolved at a very low contrast in the BB1 image, and gives rise to a so-called false resolution in the other two modes (i.e., in this case two rather than three bars).

APPENDIX C

BROADBAND IMAGES

The purpose of this appendix is to compare predictions and measurements of the cone signal-to-noise ratio. Results are intended to verify predicted variations of image quality with lighting geometry, and to illustrate some of the limitations that are inherent in the use of a single criterion to describe the quality of an image.

Figure 27 presents comparisons of predicted and measured cone signal-to-noise ratios $\langle S/N \rangle$, and images from which the measurements were obtained; figure 27(a) is for a Sun azimuth angle $\theta = 40^{\circ}$ (which was the closest to $\theta = 0^{\circ}$ that could be obtained for measurements), figure 27(b) is for $\theta = 90^{\circ}$, and figure 27(c) is for $\theta = 180^{\circ}$. Measurements of $\langle S/N \rangle$ were obtained at 10° intervals of incidence angle ι_o ranging from 30° to 80°. A cone with slope $\alpha = 30^{\circ}$ and radius $r_{cn} = 3$ cm was located at a distance of 2.7 m, corresponding to the in-focus distance of the high-resolution diode BB2. The surface material was Colorado basalt (latite), with a mean particle diameter of 220 μm. The target was illuminated by sunlight with the aid of a heliostat. (The curves shown in fig. 27 depart slightly from corresponding curves shown in fig. 19 at high incidence angles because atmospheric transmittance is independent of incidence angle when the heliostat is used.)

Evaluations of experimental results were based on computer printouts of the image data that gave the quantization level of each pixel. The evaluator first outlined the part of the cone that is brighter than the background and the other part that is darker (including shadow, if present). Then he recorded the number of pixels $n_{\pm}$ in each section and their quantization level $N_{d,i}$. The effective diameter of each cone section was taken to be

$$b_{\pm} = \sqrt{\frac{4}{\pi} N_{\pm}}$$

and the average signal excursion was taken to be

$$N_{d,\pm} = \frac{1}{n_{\pm}} \sum_{i=1}^{n_{\pm}} \left| N_{d,i} - N_{d,o} \right|$$

where $N_{d,o}$ is the background quantization level. The corresponding photosensor-array output voltages $V_{\pm}$ were computed with equation (17); the signal-to-noise ratios $\langle S/N \rangle$, with equation (45a).

APPENDIX C

Results show that measurements are in general agreement with image quality predictions. However, the images also illustrate an obvious limitation of the predictions in failing to account for the orientation of surface target shadows: Although high surface contrasts can be obtained when the camera faces the Sun, shadows obscure the side of the cone (i.e., rock) that could otherwise be observed.

REFERENCES

1. The Viking Missions to Mars. Icarus, vol. 16, no. 1, Feb. 1972.
2. The Viking Mission to Mars. NASA SP-334, 1974.
3. Huck, F. O.; McCall, H. F.; Patterson, W. R.; and Taylor, G. R.: The Viking Mars Lander Camera. Space Sci. Instrum., vol. 1, no. 2, May 1975, pp. 189-241.
4. Huck, Friedrich O.; Katzberg, Stephen J.; Jobson, Daniel J.; and Fales, Carl L., Jr.: An Analysis of the Facsimile-Camera Response to Radiant Point Sources. NASA TN D-7389, 1973.
5. Bracewell, Ron: The Fourier Transform and Its Applications. McGraw-Hill Book Co., c.1965.
6. Goodman, Joseph W.: Introduction to Fourier Optics. McGraw-Hill Book Co., Inc., c.1968.
7. Huck, Friedrich O.; Wall, Stephen D.; and Burcher, Ernest E.: An Investigation of the Facsimile Camera Response to Object Motion. NASA TN D-7668, 1974.
8. Huck, Friedrich O.; and Park, Stephen K.: Formulation of the Information Capacity of the Optical-Mechanical Line-Scan Imaging Process. NASA TN D-7942, 1975.
9. Katzberg, Stephen J.; Huck, Friedrich O.; and Wall, Stephen D.: An Investigation of Photosensor Aperture Shaping in Facsimile Cameras. NASA TN D-6882, 1972.
10. Huck, Friedrich O.; and Lambiotte, Jules J., Jr.: A Performance Analysis of the Optical-Mechanical Scanner as an Imaging System for Planetary Landers. NASA TN D-5552, 1969.
11. Hopkins, H. H.: The Frequency Response of a Defocused Optical System. Proc. Roy. Soc. (London), ser. A., vol. 231, no. 1184, July 19, 1955, pp. 91-103.
12. Born, Max; and Wolf, Emil: Principles of Optics. Third ed. Pergamon Press, c.1965.
13. Carlson, A. Bruce: Communications Systems. McGraw-Hill Book Co., c.1968.
14. Rindfleisch, T.; and Willingham, D.: A Figure of Merit Measuring Picture Resolution. Tech. Rep. No. 32-666 (Contract No. NAS 7-100), Jet Propulsion Lab., California Inst. Technol., Sept. 1, 1965. (Available as NASA CR-67187.)
15. Huck, Friedrich O.: A Lighting Strategy for Lunar Orbiter Mission Design. NASA TN D-4501, 1968.
16. Abramowitz, Milton; and Stegun, Irene A., eds.: Handbook of Mathematical Functions With Formulas, Graphs, and Mathematical Tables. NBS Appl. Math. Ser. 55, U.S. Dep. Com., June 1964, pp. 485, 556, 559.

17. Surface Models of Mars (1975). NASA SP-8020, 1975.

18. Leovy, C. B.; Briggs, G. A.; and Smith, B. A.: Mars Atmosphere During the Mariner 9 Extended Mission: Television Results. J. Geophys. Res., vol. 78, no. 20, July 10, 1973, pp. 4252-4266.

19. News Digest – Martian Color Data. Aviat. Week & Space Technol., vol. 101, no. 20, Nov. 18, 1974, p. 22.

20. Meador, Willard E.; and Weaver, Willard R.: A Photometric Function for Diffuse Reflection by Particulate Materials. NASA TN D-7903, 1975.

21. Thorpe, Thomas E.: Mariner 9 Photometric Observations of Mars From November 1971 Through March 1972. Icarus, vol. 20, no. 4, Dec. 1973, pp. 482-489.

22. Weaver, W. R.; Meador, W. E.; and Wood, G. P.: Values of the Photometric Parameters of Mars and Their Interpretation. NASA TM X-71949, 1974.

23. Huck, Friedrich O.; Burcher, Ernest E.; Taylor, Edward J.; and Wall, Stephen D.: Radiometric Performance of the Viking Mars Lander Cameras. NASA TM X-72692, 1975.

24. Stair, Ralph; Schneider, William E.; and Jackson, John K.: A New Standard of Spectral Irradiance. Appl. Opt., vol. 2, no. 11, Nov. 1963, pp. 1151-1154.

25. Measurement of Thermal Radiation Properties of Solids. NASA SP-31, 1963.

26. Wall, Stephen D.; Burcher, Ernest E.; and Jobson, Daniel J.: Reflectance Characteristics of the Viking Lander Camera Reference Test Charts. NASA TM X-72762, 1975.

TABLE I.- DESIGN AND OPERATING CHARACTERISTICS OF CAMERA

Height, cm	55.6
Diameter:	
Upper elevation assembly, cm	14.4
Lower azimuth assembly, cm	25.6
Weight, kg	7.26
Power:	
Internal calibration, W	22
Low-resolution imaging, W	34
High-resolution imaging, W	27
Standby, W	22
Thermal control (av for cold day), W	3
Slew to new command (less than 30 ms), W	111
Environment:	
Atmosphere	Earth or CO_2
Atmospheric pressure:	
Earth, mbar	1000
Cruise	Vacuum
Mars, mbar	2.8 to 20
Ambient temperature:	
Sterilization, ^{o}C	113
Mars, ^{o}C	-126 to +52
Hazards	Dust storms up to 70 m/s

TABLE II.- PERFORMANCE CHARACTERISTICS

Characteristic	Survey	Color and IR	High resolution
Instantaneous field of view, deg	0.12	0.12	0.04
Picture element registration error, deg	±0.036	±0.013	±0.006
Absolute angle error:			
Elevation, deg	±0.3	±0.2	±0.2
Azimuth, deg	±0.15	±0.1	±0.1
Frame width:			
Elevation, deg	61.44	61.44	20.48
Azimuth (min; max), deg	2.5; 342.5	2.5; 342.5	2.5; 342.5
Field of view:			
Elevation, deg	100; from 40^{o} above to 60^{o} below horizon in 10^{o} steps		
Azimuth, deg	342.5; in multiples of 2.5^{o} steps		
Geometric depth of field, m	1.7 to ∞	1.7 to ∞	1.7 to ∞
In-focus distance, m	3.7	3.7	1.9, 2.7, 4.5, and 13.3
Picture elements per line	512	512	512
Bits per picture element	6	6	6
Bits per degree azimuth	2.84×10^4	8.53×10^4	8.53×10^4
Time per degree azimuth:			
Rapid scan, s	1.84	5.52	5.52
Slow scan, min	2.0	6.0	6.0

TABLE III.- TYPICAL PICTURE FORMATS: THEIR NUMBER OF BITS AND TIMES NECESSARY TO OBTAIN AND TRANSMIT DATA AT 16 000 bits/s

Average amount of imagery data transmitted per day:
Nominal mission: 10×10^6 bits recorded, 6×10^6 bits real time
Preprogramed mission: 10×10^6 bits

Imaging mode	Time, min	Data, bits
Survey:		
$60^o \times 60^o$	1.84	1.7×10^6
$60^o \times 120^o$	3.68	3.4
$60^o \times 240^o$	7.36	6.8
$60^o \times 360^o$	11.04	10.2
Multispectral (color or IR):		
$60^o \times 60^o$	5.52	5.1×10^6
$60^o \times 120^o$	11.04	10.2
High resolution:		
$20^o \times 20^o$	1.84	1.7×10^6
$20^o \times 60^o$	5.52	5.1
$20^o \times 120^o$	11.04	10.2

TABLE IV.- TYPICAL NOISE-EQUIVALENT RADIANCES FOR ALL GAINS AND SCAN RATES

Scan rate	Gain number	Noise-equivalent radiance, W/m^2-sr, for channel –							
		High resolution	Survey	Blue	Green	Red	IR1	IR2	IR3
Slow	0	0.013	0.008	0.014	0.013	0.010	0.011	0.013	0.011
	1	.019	.016	.020	.019	.018	.018	.019	.017
	2	.035	.032	.036	.032	.035	.033	.033	.030
	3	.067	.064	.068	.062	.070	.065	.063	.059
	4	.133	.128	.135	.122	.141	.130	.124	.118
	5	.265	.256	.270	.243	.281	.259	.247	.235
Rapid	0	0.069	0.019	0.080	0.076	0.040	0.055	0.073	0.058
	1	.070	.024	.081	.077	.043	.056	.074	.059
	2	.076	.036	.086	.081	.053	.063	.079	.064
	3	.095	.066	.104	.097	.080	.084	.095	.082
	4	.149	.129	.156	.143	.146	.140	.143	.131
	5	.274	.257	.281	.254	.284	.264	.257	.242

TABLE V.- ILLUMINATION SCATTERING PARAMETERS OF FOUR SURFACES

Surface	Physical parameters		
	a_0	a_1	a_2
Mars (Thorpe)	0.55	0.60	0.18
Colorado basalt (mean particle diameter of 220 μm)	-.10	.26	.15
Strong backscatter	.8	.1	.1
Near-Lambertian reflectance	-.8	3.0	.5

TABLE VI.- MAXIMUM SIGNAL LEVELS FOR FOUR SURFACE ALBEDOS

Surface albedo	Maximum photosensor-array output voltage, V, for channel –						
	Broadband	Color			Near-infrared		
		Blue	Green	Red	IR1	IR2	IR3
ρ_1	2.40	1.87	2.45	2.31	2.42	2.57	2.72
ρ_2	1.74	1.43	1.81	1.68	1.82	1.93	2.03
ρ_3	1.24	1.24	1.39	1.15	1.27	1.35	1.40
ρ_4	.89	1.11	1.14	.86	.77	.81	.89

TABLE VII.- V/N FOR SEVERAL SURFACE ALBEDOS AND BROADBAND IMAGING MODES

Gain number	Imaging mode	V/N for albedo –			
		ρ_1	ρ_2	ρ_3	ρ_4
3	High resolution, rapid scan				121
	High resolution, slow scan				172
	Survey, rapid scan				173
4	High resolution, rapid scan		151	108	77
	High resolution, slow scan		170	121	87
	Survey, rapid scan		175	124	89
5	High resolution, rapid scan	111	82	59	42
	High resolution, slow scan	115	85	60	43
	Survey, rapid scan	119	88	62	45

TABLE VIII.- SUMMARY OF BROADBAND IMAGE QUALITY PREDICTIONS

Figure	Image-quality criteria	V/N	Lighting geometry[a]		Cone		Scattering characteristics[b]
			Incidence, ι_o, deg	Azimuth, θ, deg	Slope, α, deg	Diameter, c, pixels	
19	⟨S/N⟩	----------	Variable	0, 90, 180	10, 30, 60	6	Mars (Thorpe)
	⟨c⟩	50, 100, 200			30	---	
	⟨α⟩	50, 100, 200			--------	6	
20	⟨S/N⟩	100	Variable	Variable	30	6	Mars (Thorpe)
	⟨c⟩				30	---	
	⟨α⟩				--------	6	
21	⟨S/N⟩	----------	Variable	0, 90, 180	10, 30, 60	6	All four
22	⟨S/N⟩	----------	40, 60, 80	Variable	10, 30, 60	6	All four
23	⟨S/N⟩	----------	Variable	Variable	30	6	All four

[a]See figure 13. The emittance angle ϵ_o is 60°.

[b]See figures 16 and 17.

TABLE IX.- TRANSMITTANCE OF OPTICS AND RESPONSIVITIES OF PHOTOSENSOR ARRAY

λ, μm	Transmittance			Responsivity, A/W, of channel –										
	τ_{cw}, τ_w	γ	τ_ℓ	BB1	BB2	BB3	BB4	Survey	Blue	Green	Red	IR1	IR2	IR3
0.400	0.926	0.692	0.931	0.096	0.095	0.096	0.104	0.097	0.044	0.001	0.005	0.002	0.002	0.005
.425	.930	.774	.945	.127	.125	.129	.132	.126	.082	.001	.004	.001	.001	.003
.450	.932	.783	.959	.150	.149	.159	.163	.151	.120	.001	.002	.001	.001	.005
.475	.934	.820	.964	.174	.172	.187	.188	.175	.142	.003	.001	.001	.002	.009
.500	.940	.857	.963	.197	.196	.212	.215	.198	.120	.044	.001	.000	.008	.014
.525	.940	.846	.966	.204	.201	.221	.224	.210	.004	.108	.001	.000	.017	.008
.550	.945	.844	.954	.214	.215	.235	.240	.224	.001	.186	.001	.000	.007	.005
.575	.945	.837	.953	.232	.236	.259	.266	.248	.001	.082	.003	.001	.001	.005
.600	.949	.817	.955	.247	.253	.279	.286	.267	.001	.017	.053	.001	.001	.006
.625	.948	.819	.950	.264	.270	.297	.306	.285	.002	.003	.252	.001	.001	.008
.650	.950	.800	.943	.276	.282	.310	.317	.296	.014	.001	.251	.001	.001	.010
.675	.949	.795	.942	.282	.290	.321	.327	.306	.037	.001	.265	.001	.001	.015
.700	.949	.790	.947	.291	.298	.330	.335	.316	.005	.001	.293	.000	.001	.022
.725	.948	.767	.934	.297	.307	.338	.345	.326	.001	.001	.187	.001	.002	.029
.750	.948	.744	.945	.307	.315	.345	.352	.332	.001	.000	.040	.001	.005	.042
.775	.947	.749	.926	.315	.323	.354	.364	.343	.000	.002	.024	.006	.007	.007
.800	.948	.731	.920	.320	.328	.359	.367	.351	.002	.002	.010	.030	.002	.002
.825	.947	.785	.916	.321	.330	.364	.375	.358	.000	.000	.007	.128	.002	.002
.850	.947	.782	.914	.319	.327	.358	.370	.356	.000	.000	.003	.290	.002	.002
.875	.944	.794	.904	.306	.314	.343	.353	.344	.000	.000	.007	.226	.005	.003
.900	.943	.815	.895	.286	.293	.319	.329	.328	.001	.000	.001	.272	.025	.008
.925	.945	.835	.892	.265	.272	.297	.305	.309	.000	.001	.000	.101	.220	.028
.950	.945	.849	.890	.240	.244	.267	.275	.285	.001	.001	.000	.026	.270	.117
.975	.947	.863	.882	.209	.213	.235	.239	.253	.003	.001	.000	.011	.138	.212
1.000	.941	.870	.869	.159	.162	.179	.181	.195	.002	.003	.000	.006	.027	.169
1.025	.945	.876	.873	.112	.114	.128	.127	.140	.002	.002	.001	.004	.010	.121
1.050	.942	.880	.862	.067	.067	.078	.075	.083	.004	.002	.001	.003	.005	.072
1.075	.942	.880	.861	.035	.034	.040	.038	.043	.018	.006	.000	.003	.004	.038
1.100	.941	.881	.864	.018	.018	.021	.019	.021	.014	.016	.000	.004	.004	.020

TABLE X.- ELECTRICAL CHARACTERISTICS OF PHOTOSENSOR ARRAY

Channel	k_c	R_f, MΩ	R_i, Ω	Channel gain	r_p, μm	Diode noise, $fA/\sqrt{Hz}$	Preamplifier noise, $fA/\sqrt{Hz}$	Total noise, $fA/\sqrt{Hz}$
BB1	1.18	723.5	5 178	19.31	19.4	5.98	4.97	7.78
BB2	1.17	699.7	5 680	17.61	20.3	6.25	5.09	8.07
BB3	1.18	724.9	5 958	16.78	19.7	6.06	4.80	7.74
BB4	1.19	740.8	6 480	15.43	19.4	5.98	5.25	7.97
Survey	1.18	756.8	54 540	1.83	58.8	18.09	4.96	18.76
Blue	1.35	735.0	4 392	22.77	59.4	4.97	4.58	6.77
Green	1.39	709.5	4 082	24.50	58.8	4.64	5.07	6.89
Red	1.07	764.1	14 240	7.02	59.1	8.77	4.81	10.01
IR1	1.09	719.5	7 064	14.16	58.2	6.14	4.98	7.92
IR2	1.26	707.1	4 561	21.93	58.8	5.18	5.17	7.33
IR3	1.32	752.2	6 037	16.56	58.8	5.75	4.83	7.52

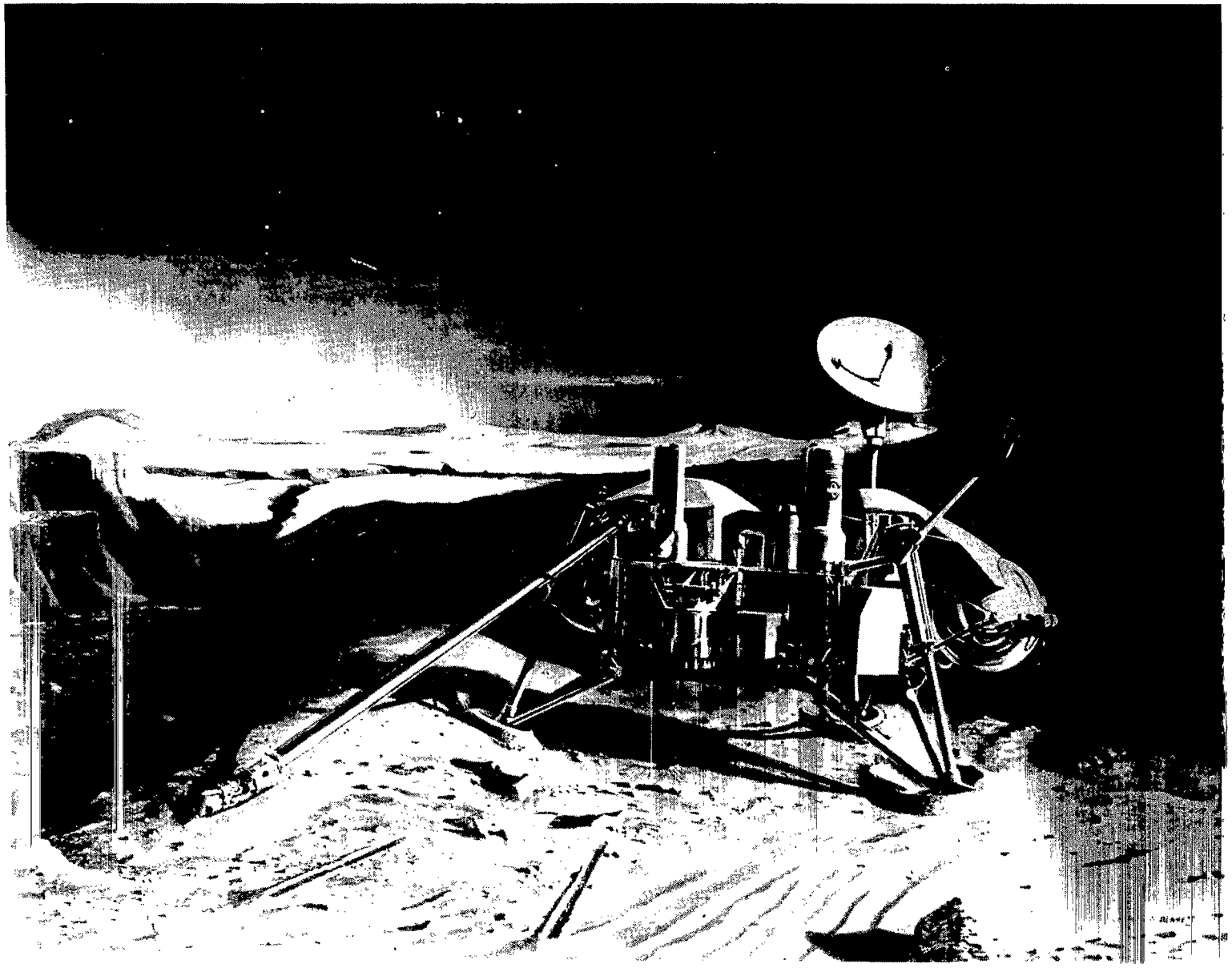

L-76-148

Figure 1.- Artist's view of Viking lander.

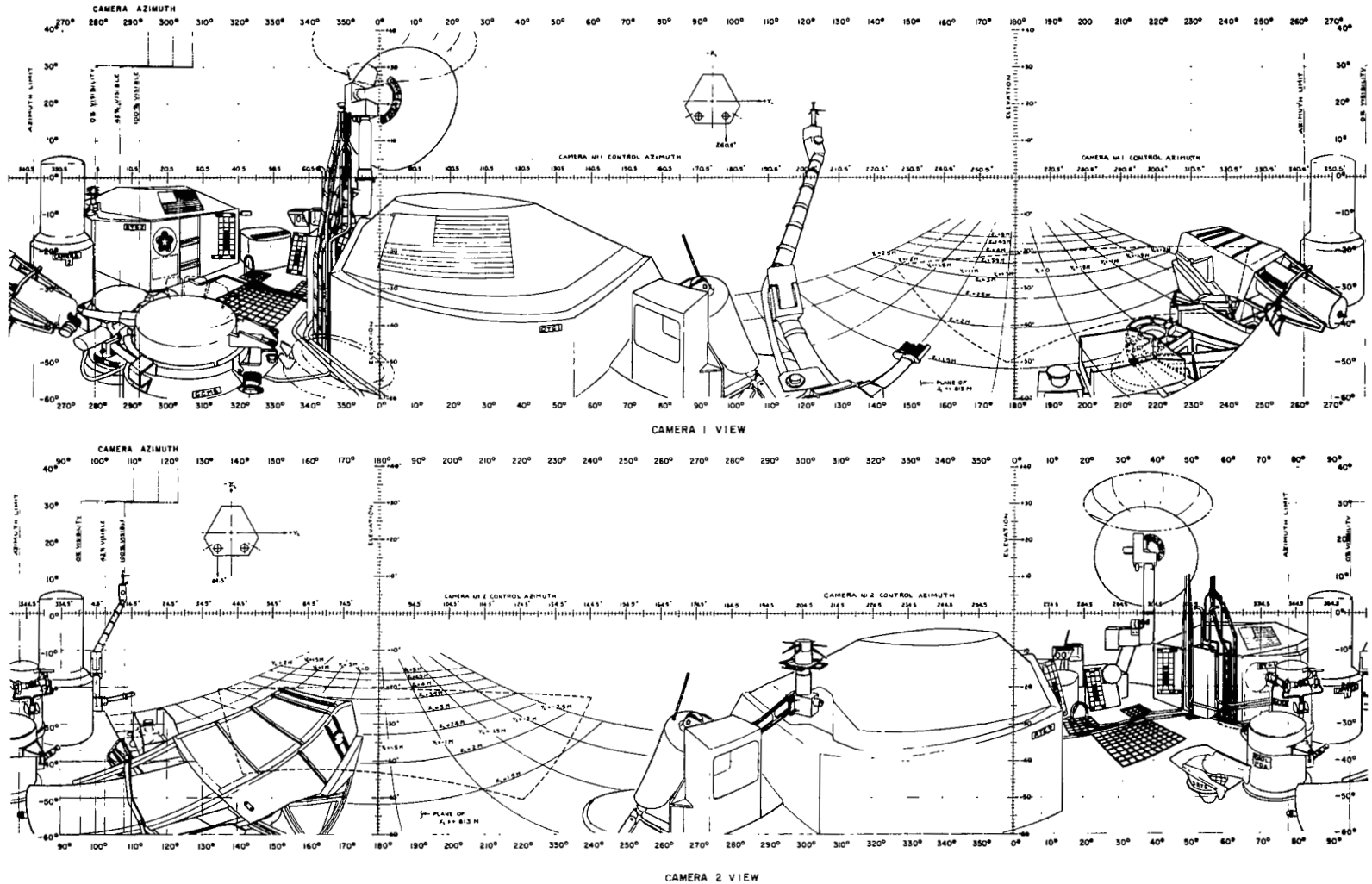

Figure 2.- Field of view of Viking lander cameras. (From U.S. Geological Survey, Oct. 1974.)

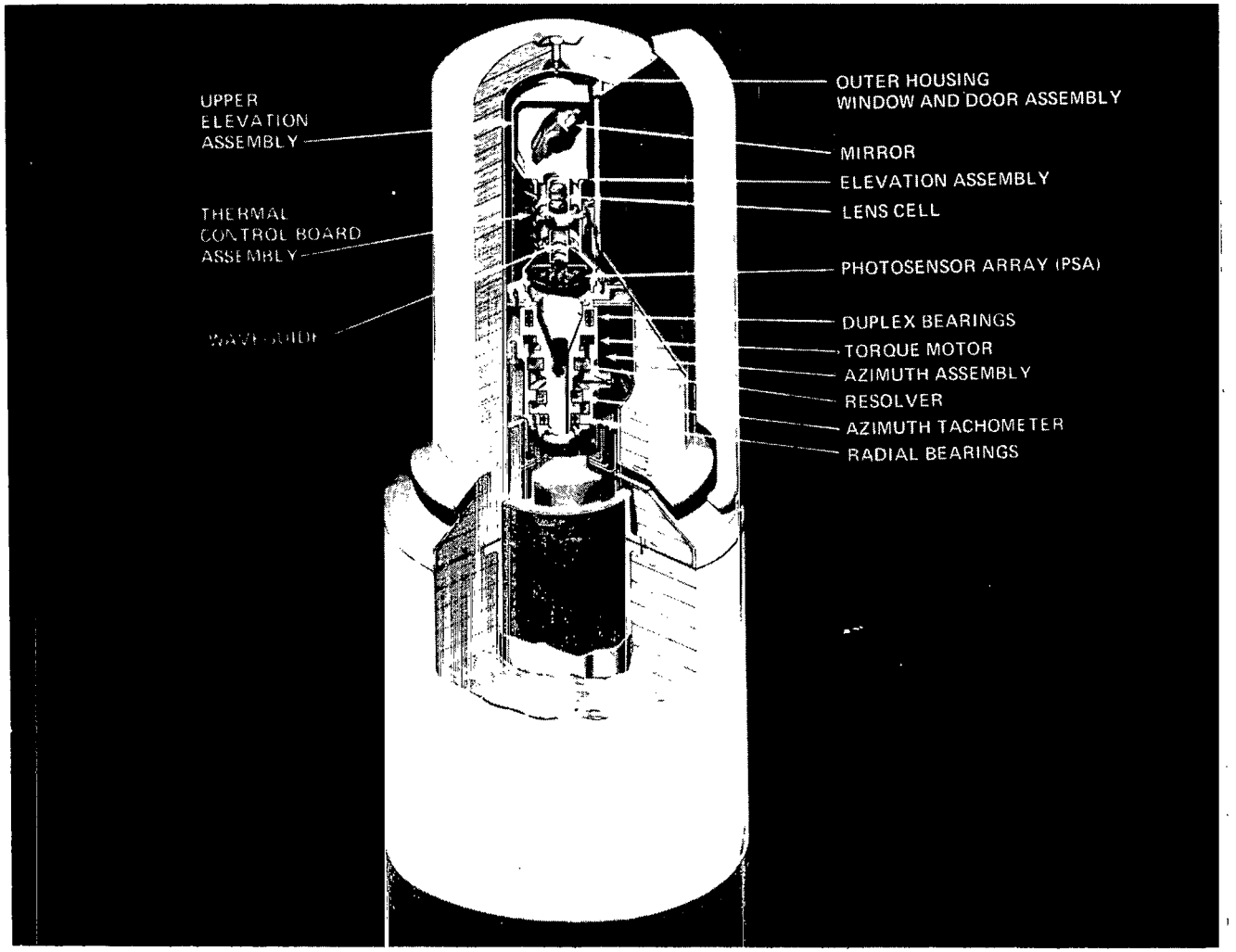

L-76-149

Figure 3.- Simplified cutaway view of Viking lander camera.

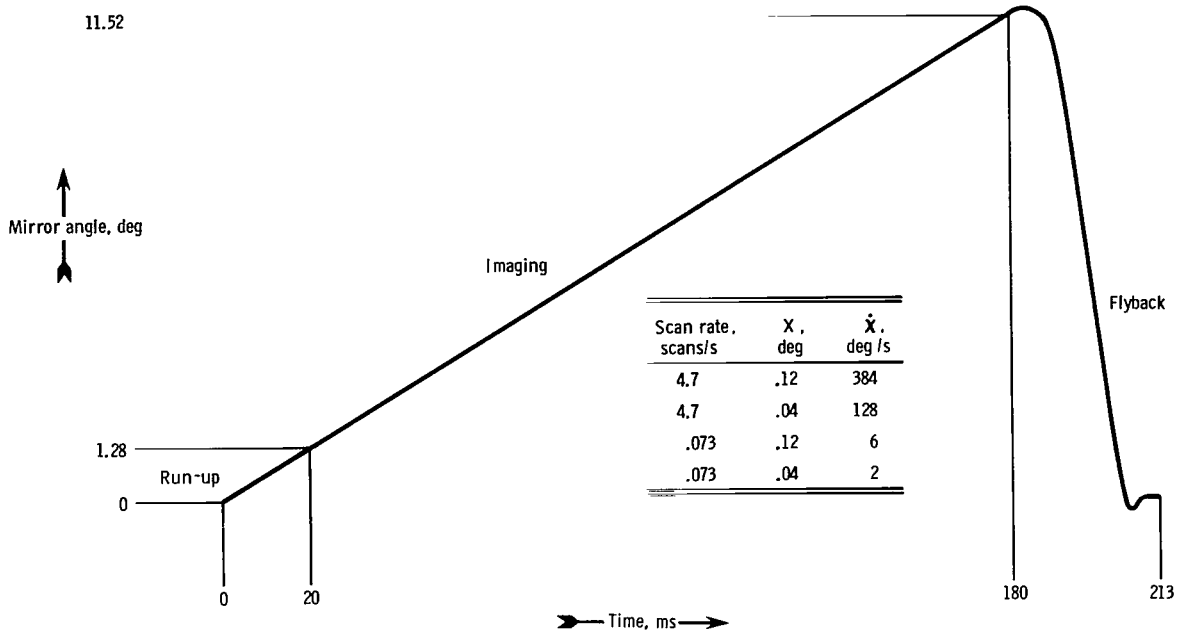

Scan rate, scans/s	X, deg	$\dot{X}$, deg /s
4.7	.12	384
4.7	.04	128
.073	.12	6
.073	.04	2

Figure 4.- Elevation scan profile. Angular and time values are given for the high-resolution (X = 0.04°) and rapid-scan (4.7 scans/s) mode; angular values are to be multiplied by 3 for low-resolution (X = 0.12°) imaging, and time values are to be multiplied by 64 for the slow scan rate (0.073 scans/s).

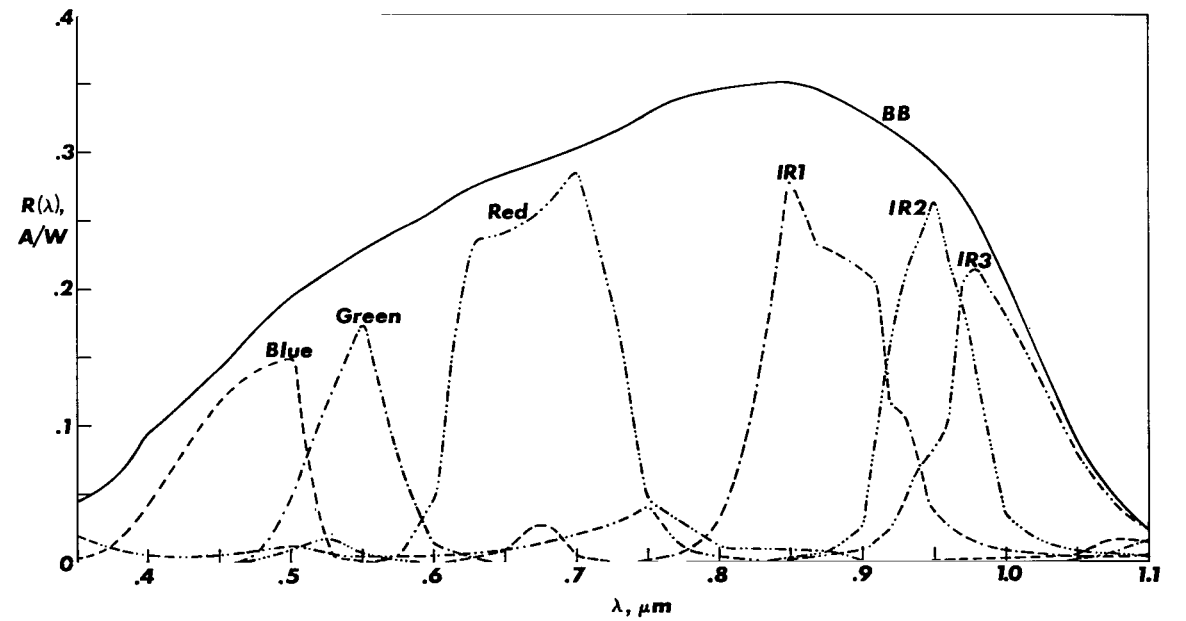

Figure 5.- Spectral responsivities of photosensor array.

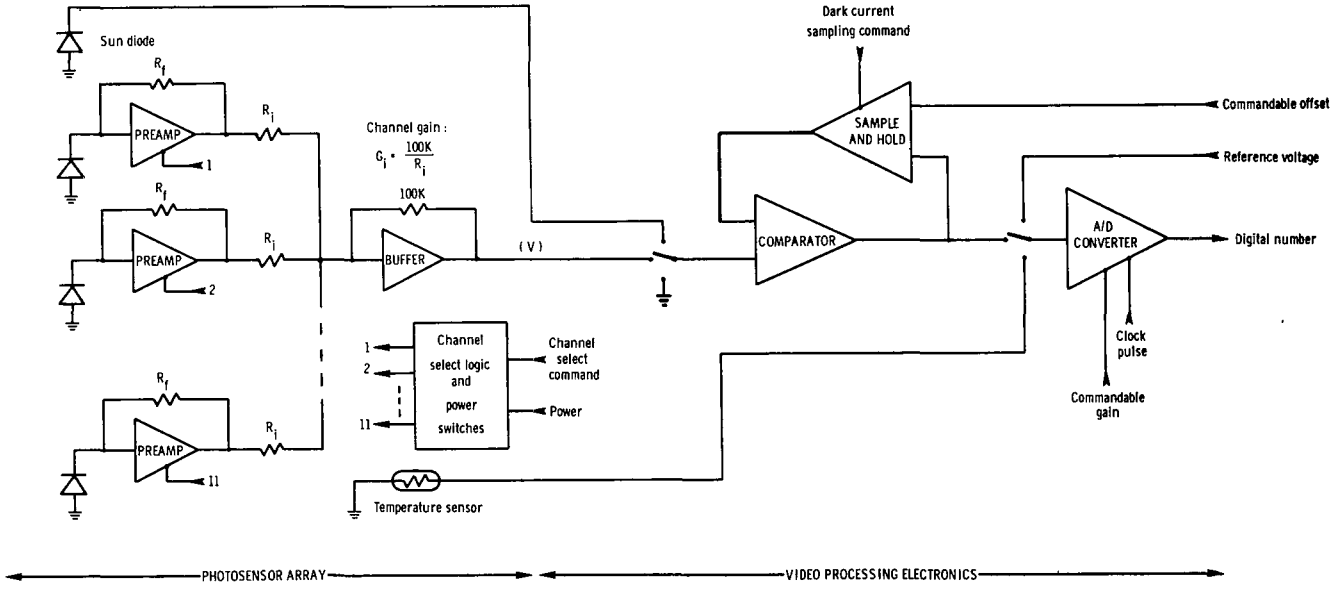

Figure 6.- Simplified circuit diagram of photosensor array and video electronics.

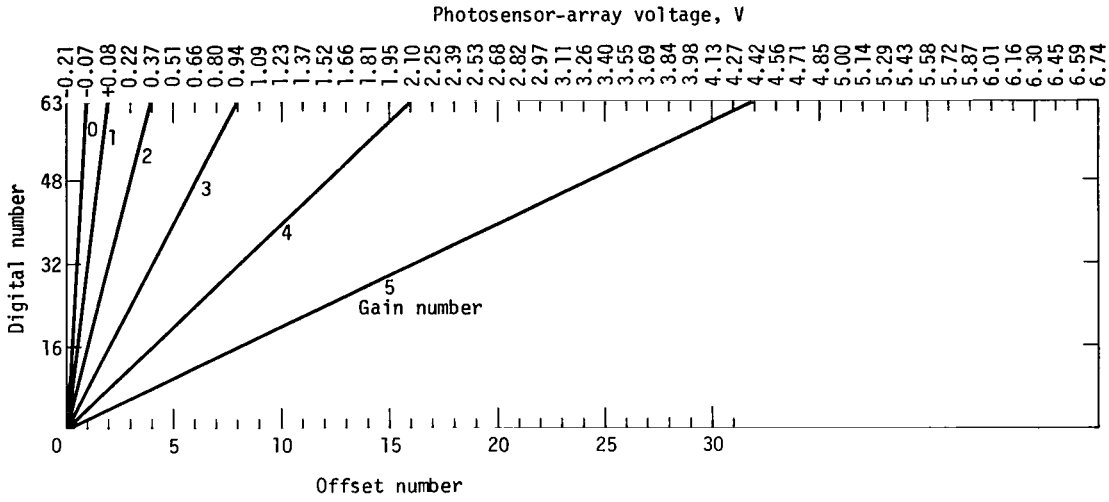

Figure 7.- Commandable gains and offsets.

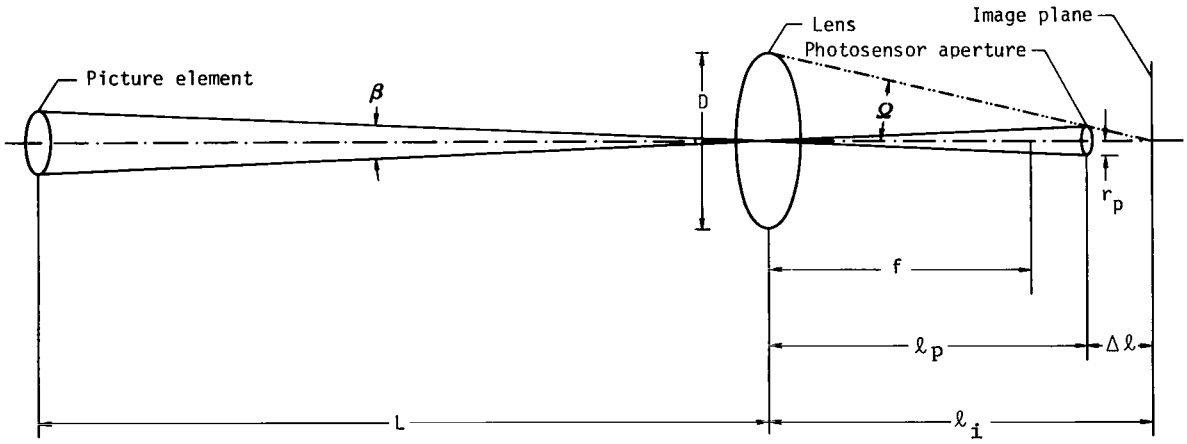

Figure 8.- Optical geometry.

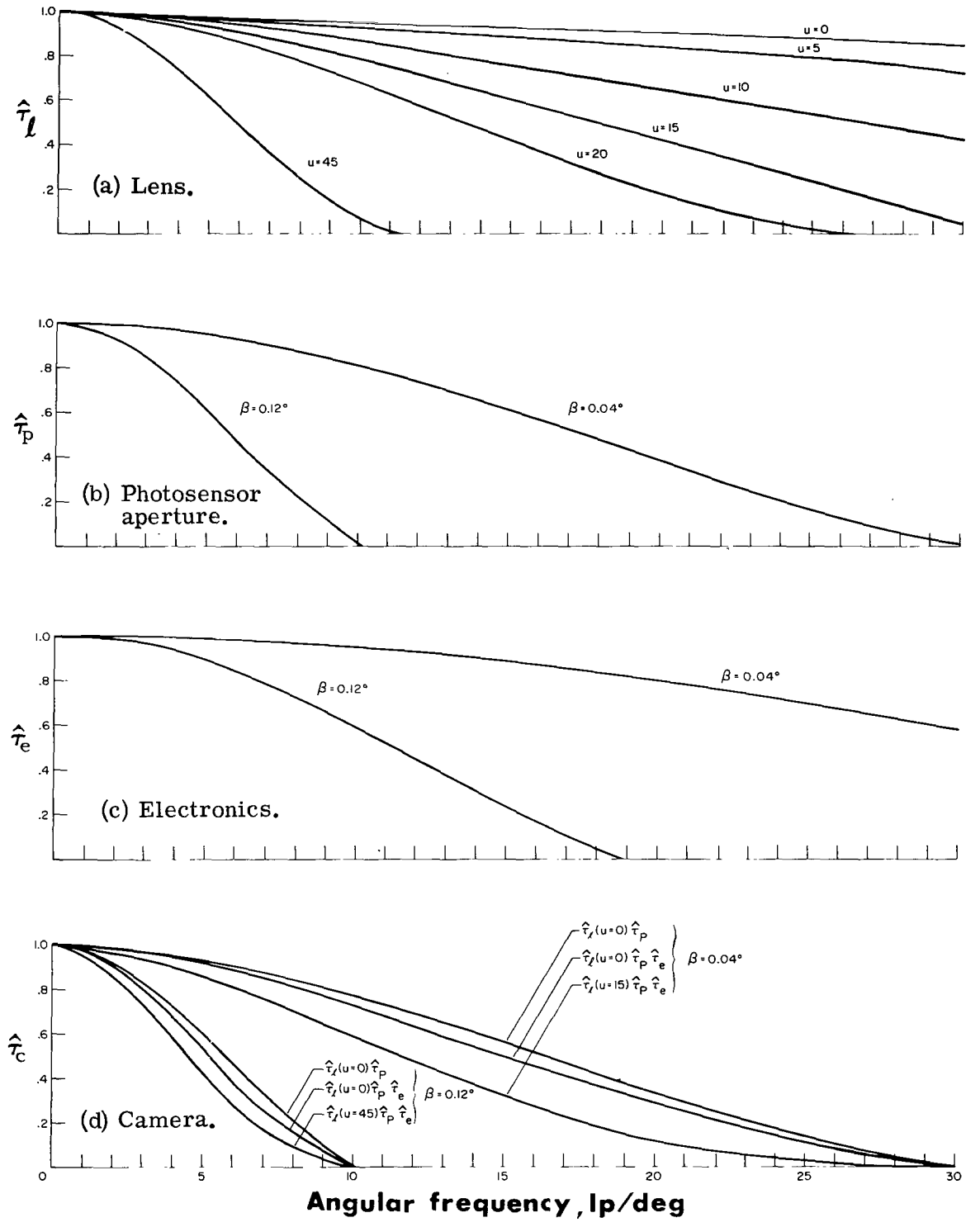

Figure 9.- Spatial frequency response. u = 45 represents maximum defocus blur for low-resolution imaging ($\beta = 0.12^{o}$) over the range from 1.7 m to ∞; u = 15, for high-resolution imaging ($\beta = 0.04^{o}$) over the same range if the best-focused diode is used at each distance.

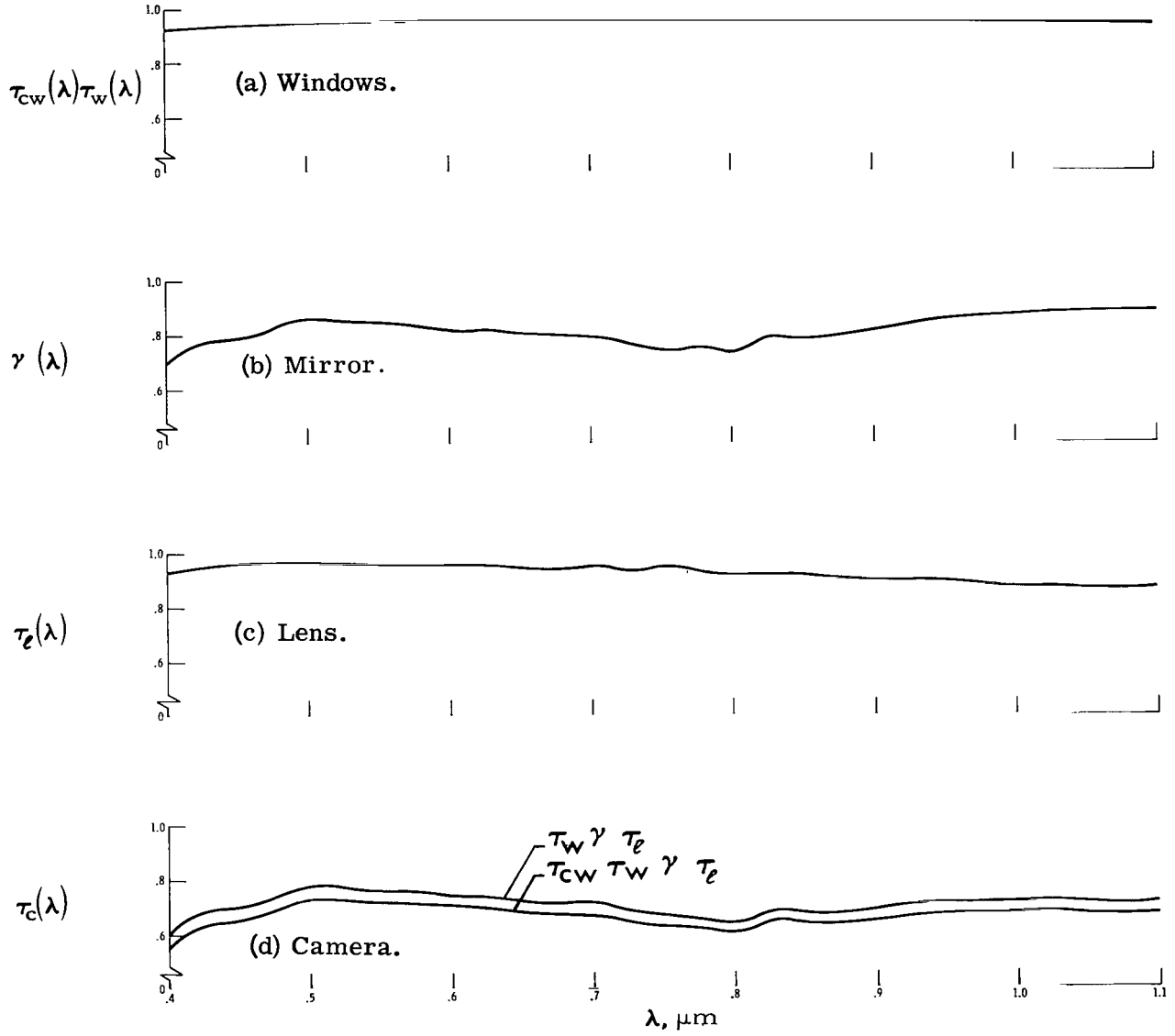

Figure 10.- Optical throughput.

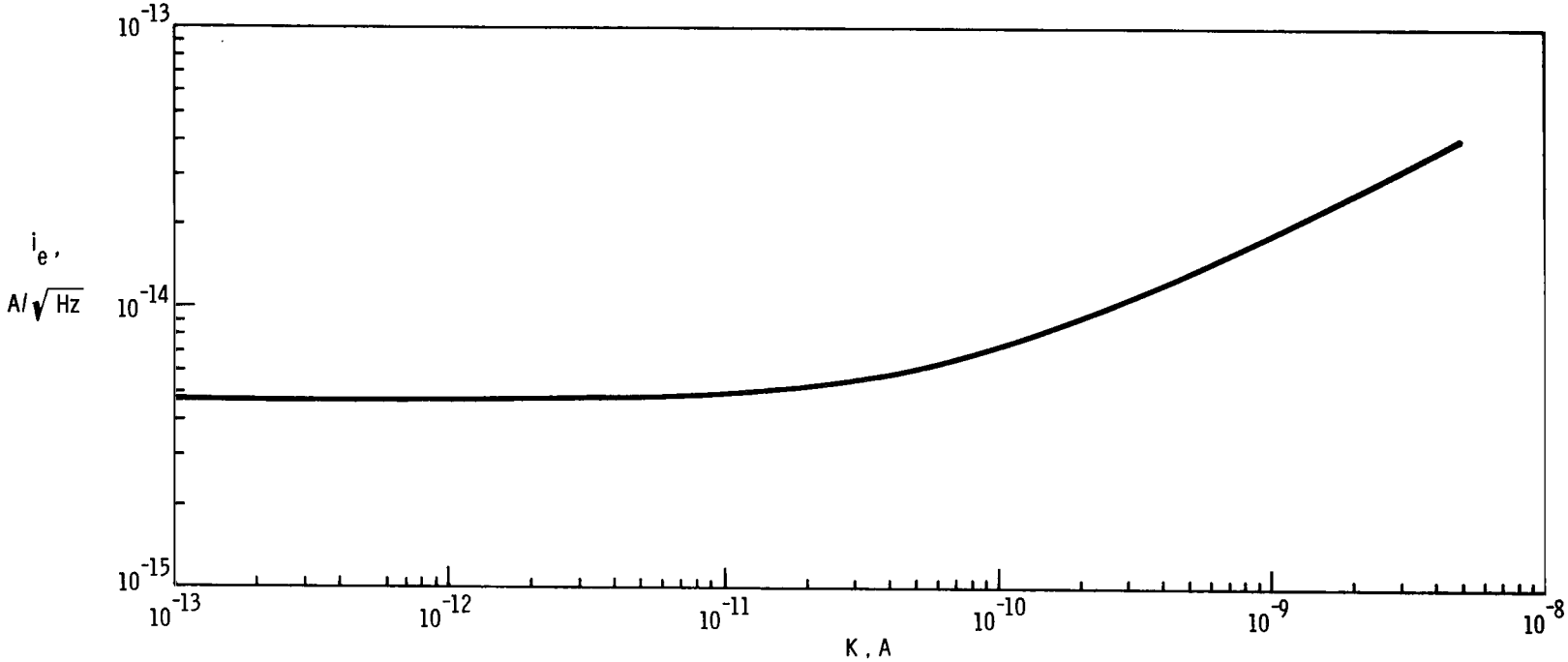

Figure 11.- Noise-current density of photosensor array.

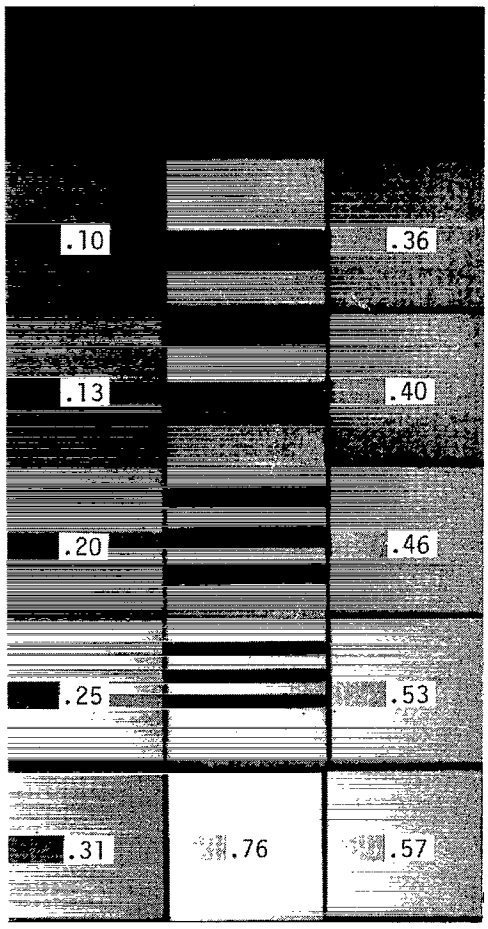

L-74-2406.1

Figure 12.- Reference test chart. (Numbers in patches are reflectances.)

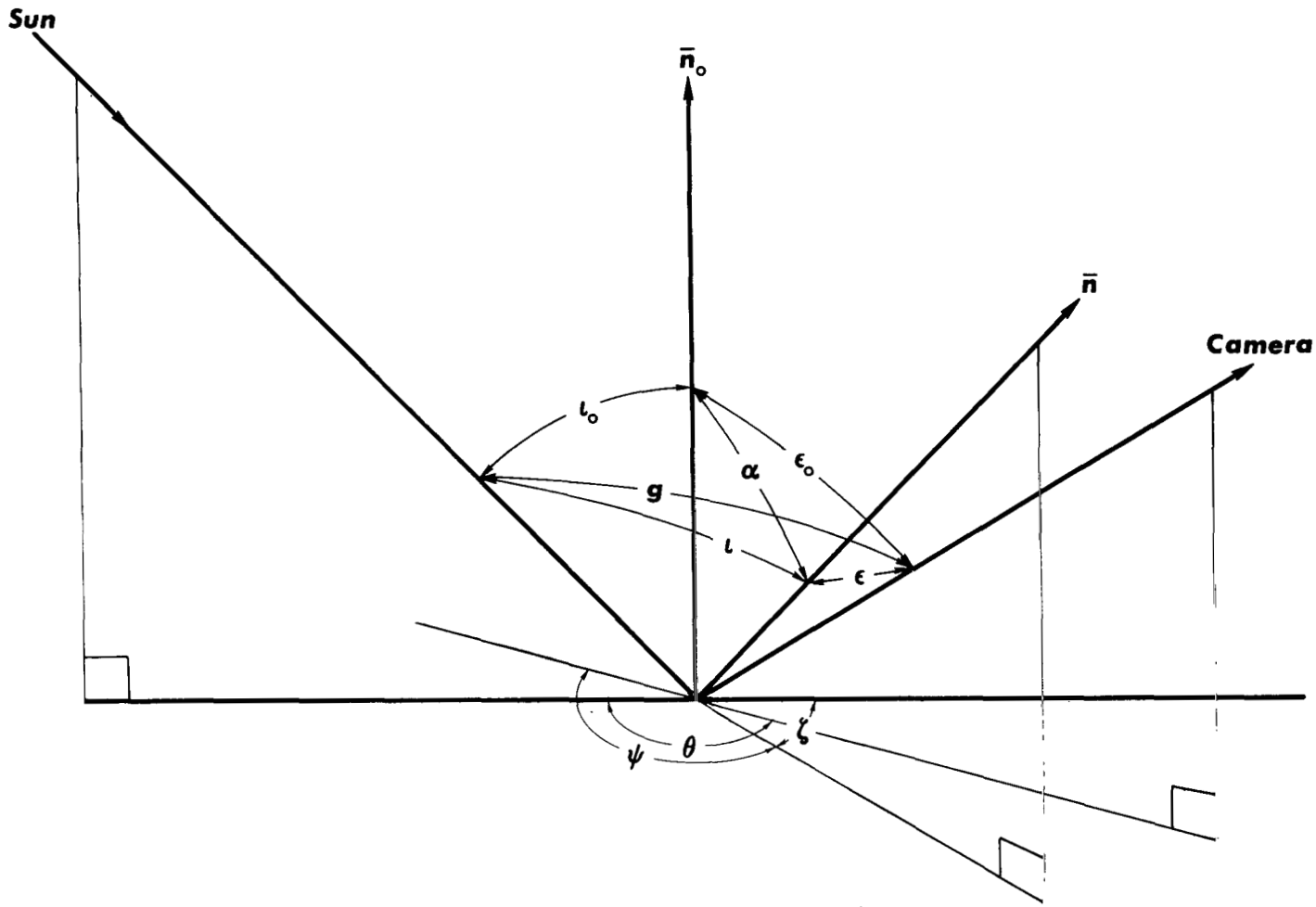

Figure 13.- Lighting and viewing geometry.

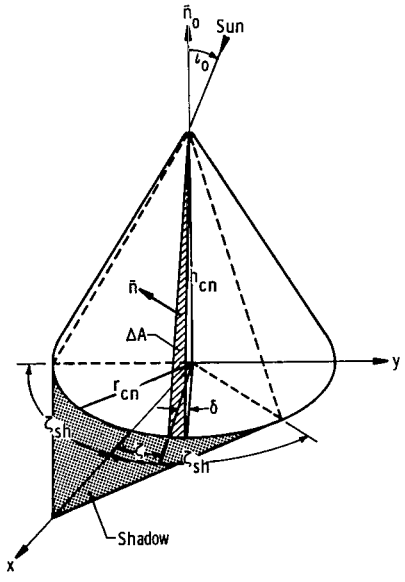

(a) Geometry for incident radiation.

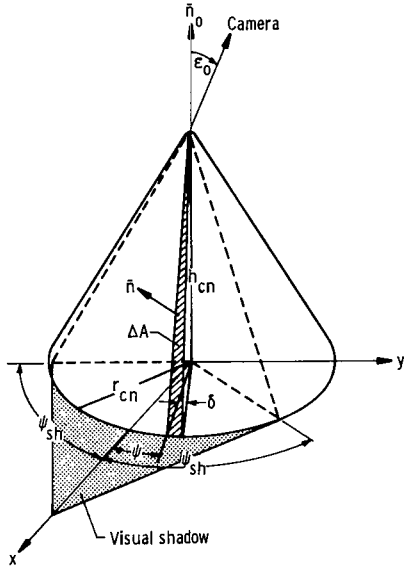

(b) Geometry for emitted radiation.

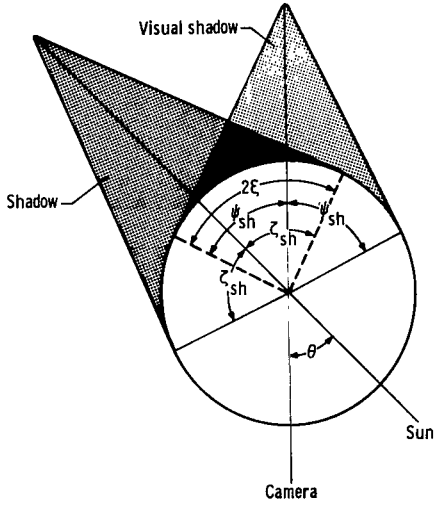

(c) Top view of cone geometry.

Figure 14.- Cone geometry.

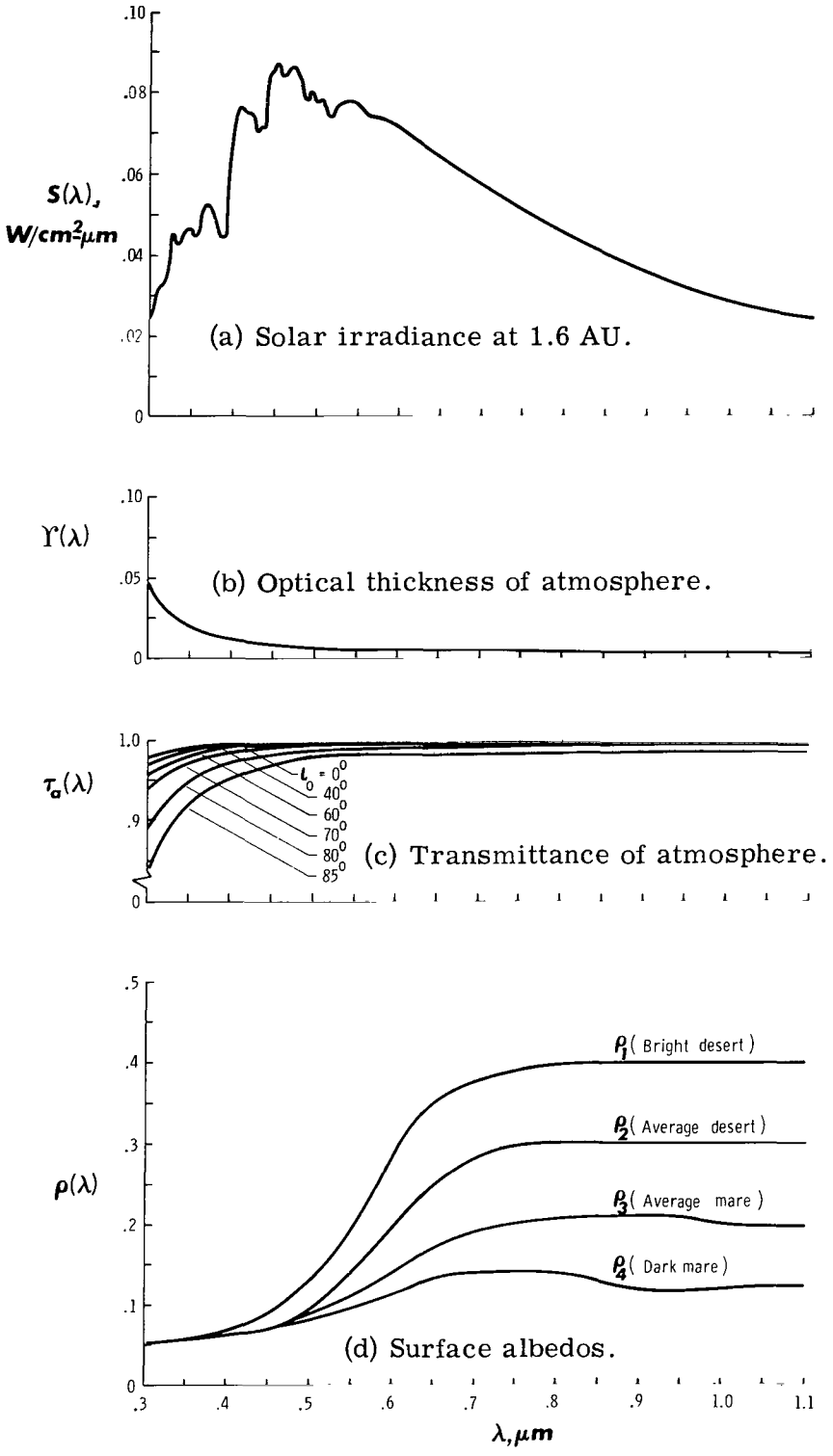

Figure 15.- Mars spectral radiance.

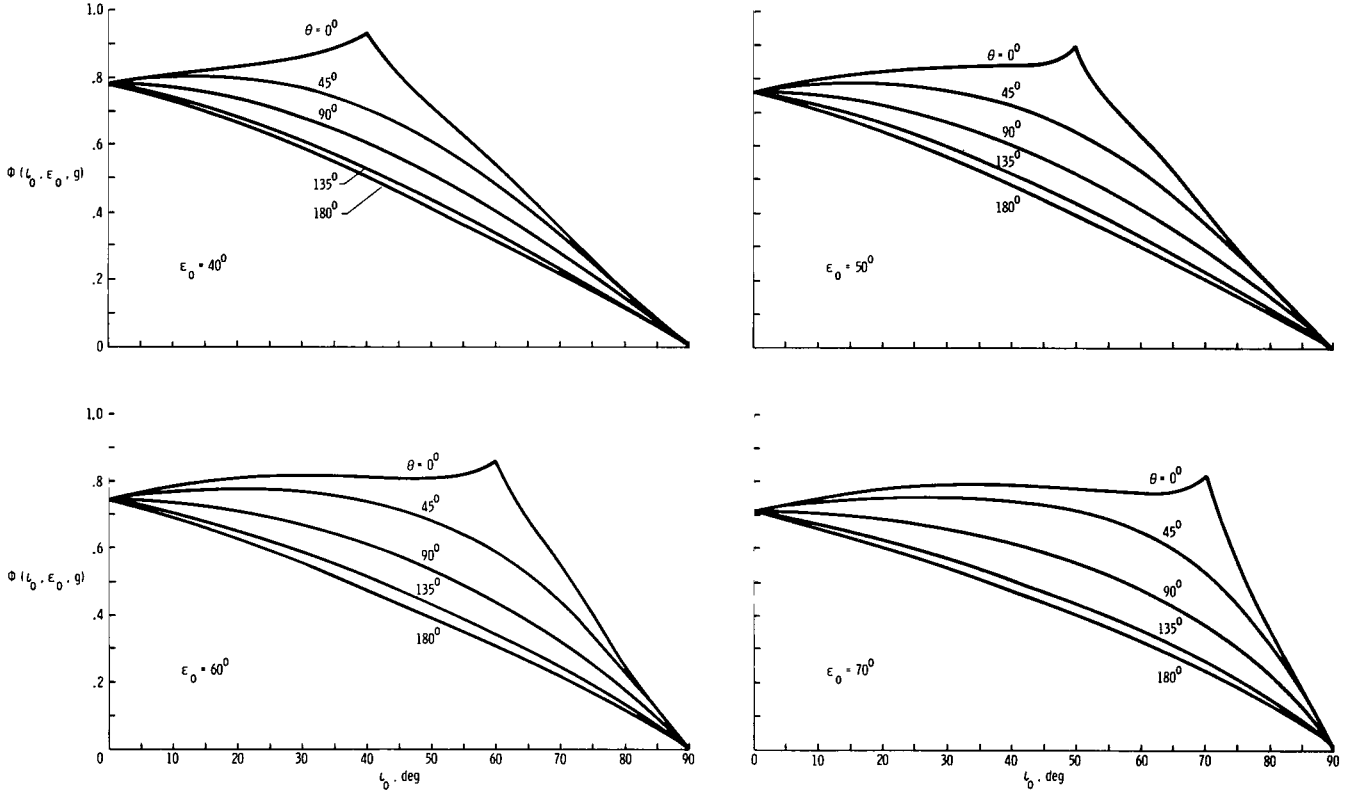

Figure 16.- Variation of Mars (Thorpe) illumination scattering characteristics with light incidence angle ι_0. Emittance angles ϵ_0 are 40^o, 50^o, 60^o, and 70^o.

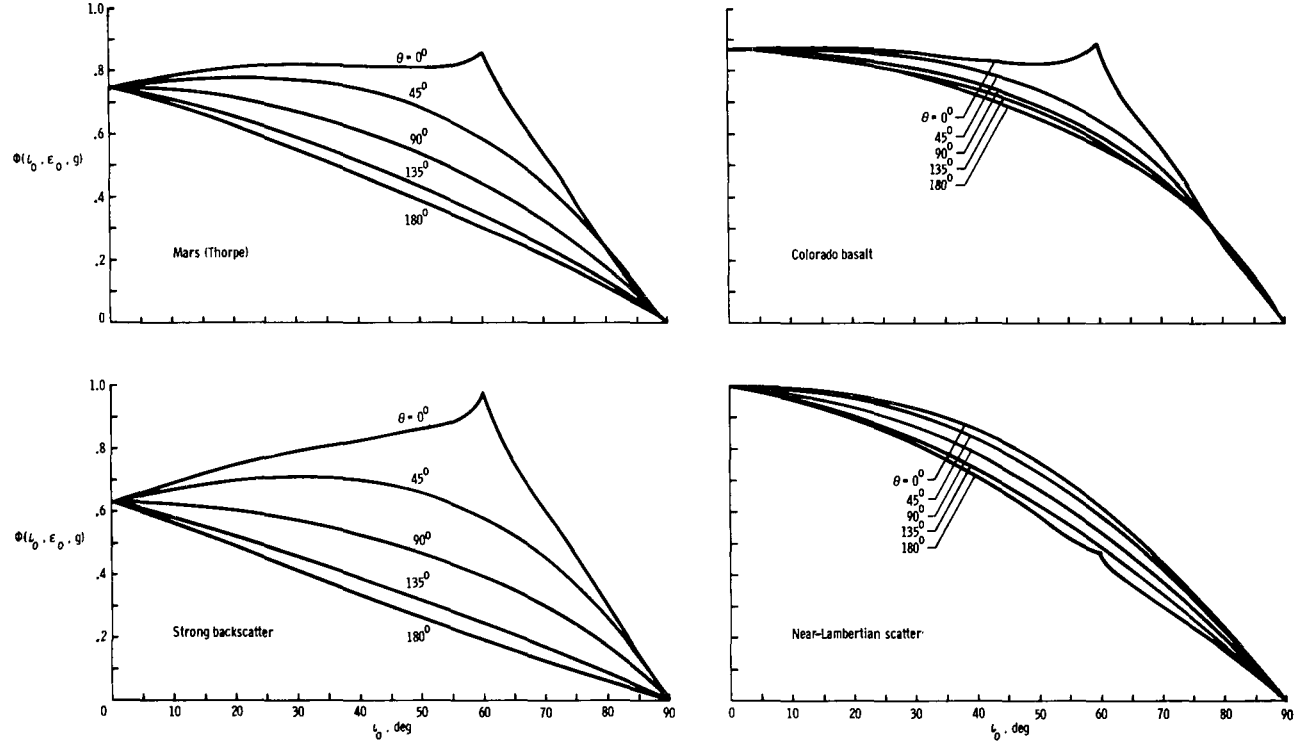

Figure 17.- Variation of four illumination scattering characteristics with light incidence angle ι_o. Emittance angle ϵ_o is 60^o.

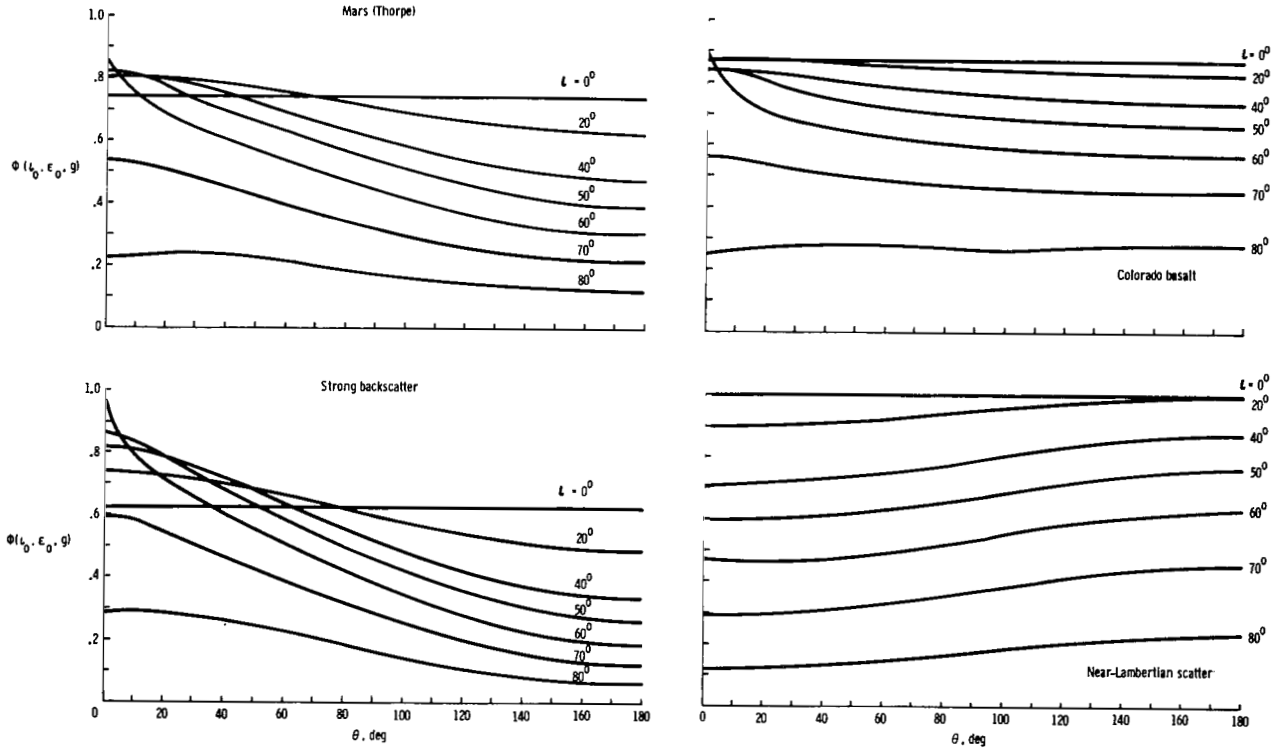

Figure 18.- Variation of four illumination scattering characteristics with azimuth angle θ between light incidence and emittance angles. Incidence angles ι_0 range from 0^o to 80^o; emittance angle ϵ_0 is 60^o.

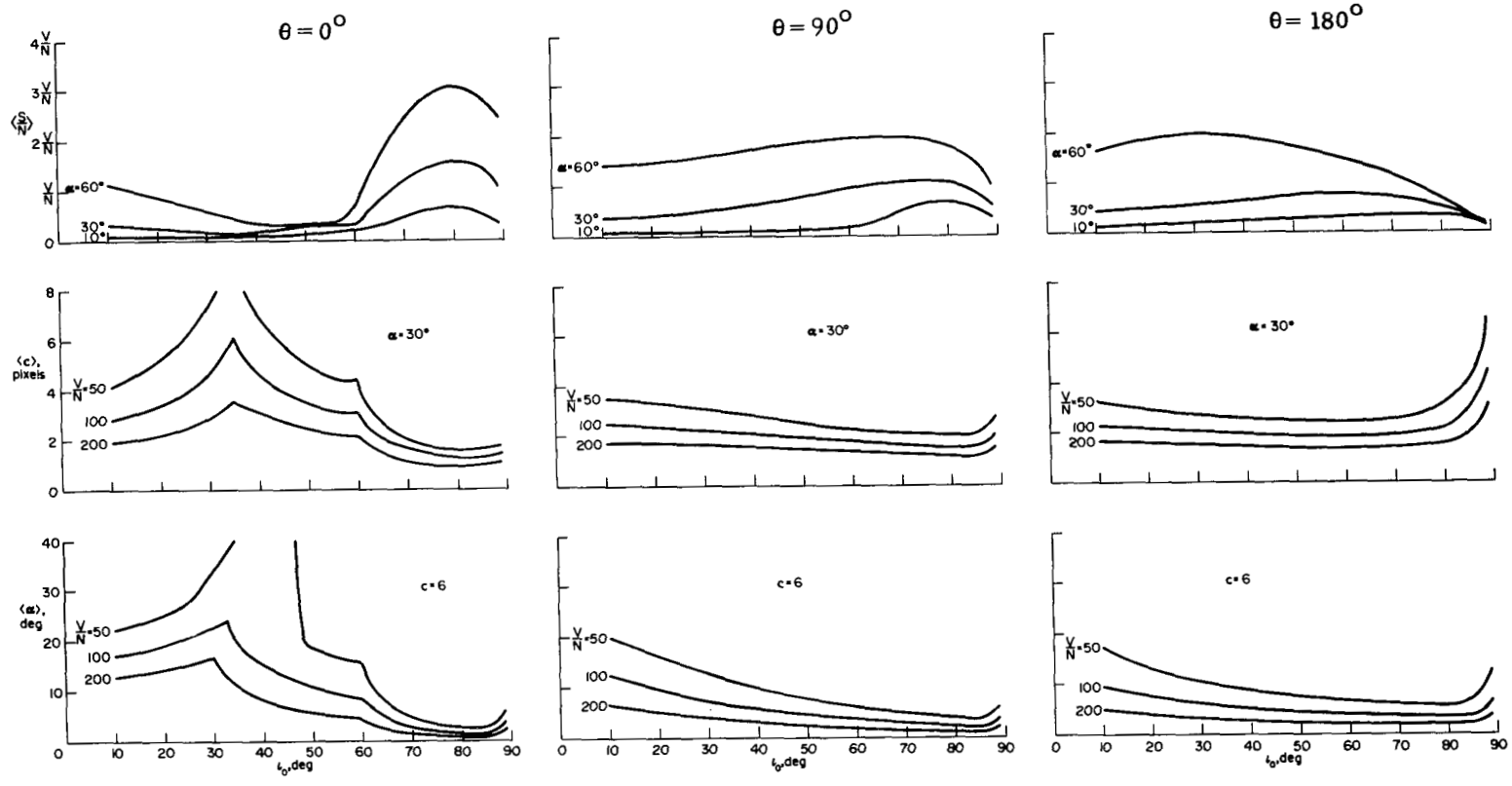

Figure 19.- Variation of image quality $\left(\langle S/N \rangle, \langle c \rangle, \text{ and } \langle \alpha \rangle\right)$ with light incidence angle ι_o for Thorpe's illumination scattering function of Mars. Azimuth angles θ are 0^o, 90^o, and 180^o; emittance angle ϵ_o is 60^o (i.e., camera elevation angle of -30^o).

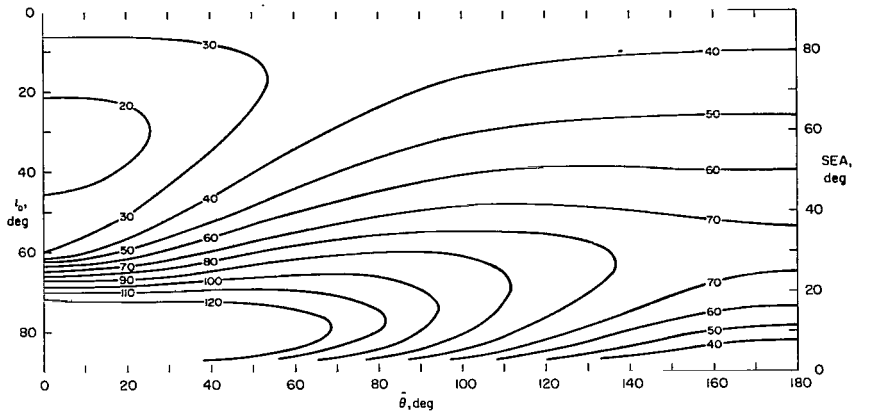

(a) Cone signal-to-noise ratio $\langle S/N \rangle$. $\alpha = 30^o$; c = 6 pixels.

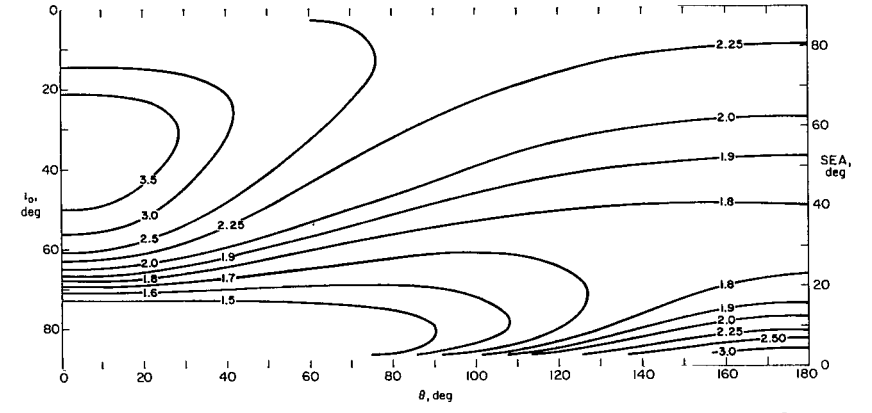

(b) Minimum detectable cone diameter $\langle c \rangle$. $\alpha = 30^o$.

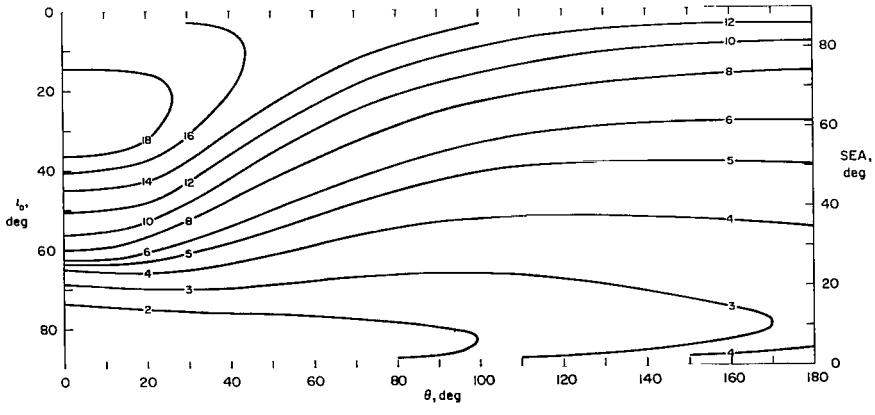

(c) Minimum detectable cone slope $\langle \alpha \rangle$. c = 6.

Figure 20.- Contour plots of image quality as a function of light incidence angle ι_o (or Sun elevation angle SEA) and azimuth angle θ for Thorpe's illumination scattering function of Mars. Emittance angle ϵ_o is 60^o (i.e., camera elevation angle of -30^o); imaging condition is adequate, V/N = 100.

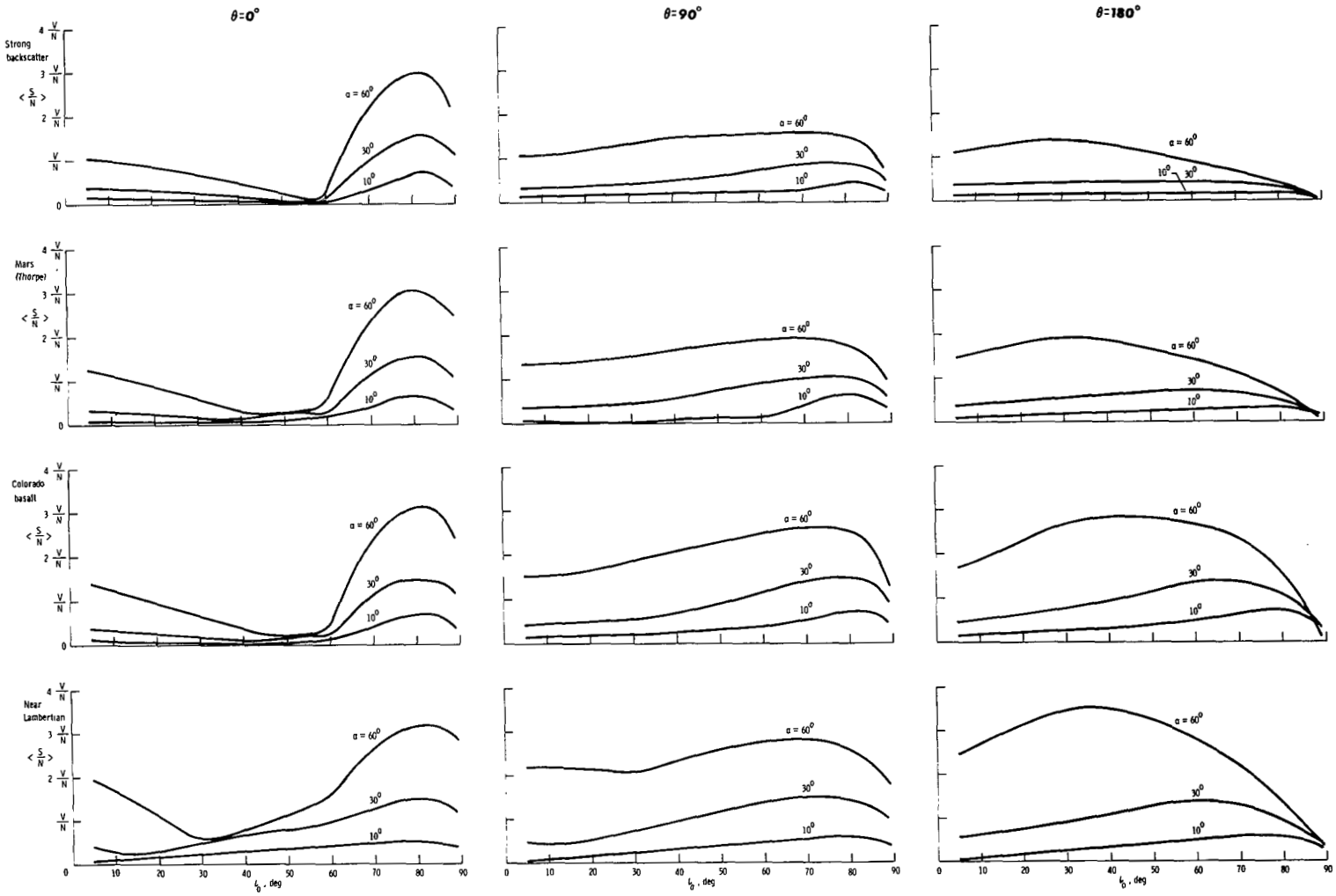

Figure 21.- Variation of cone signal-to-noise ratio $\langle S/N \rangle$ with light incidence angle ι_0. Plots are given for three azimuth angles θ and four illumination scattering characteristics.

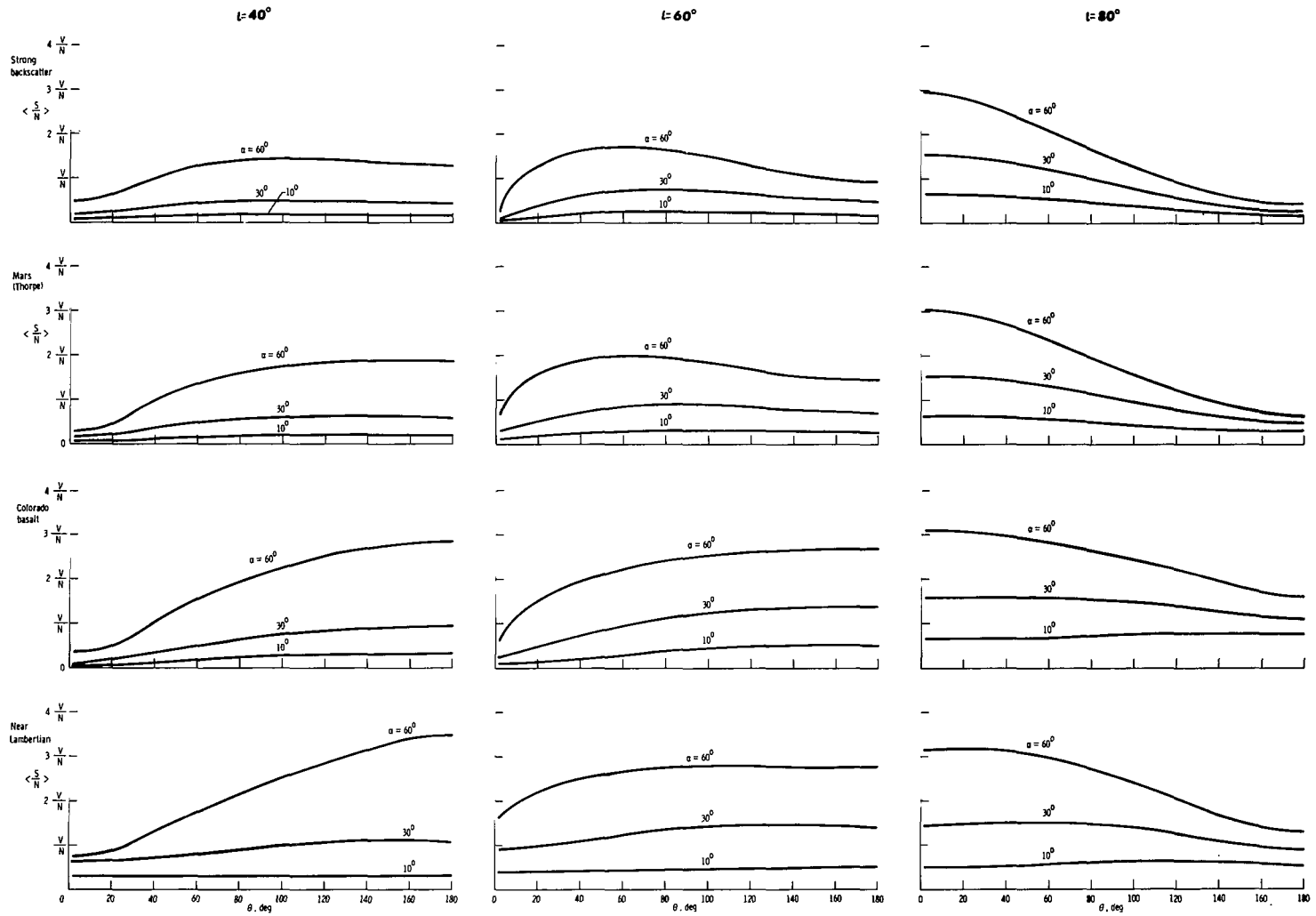

Figure 22.- Variation of cone signal-to-noise ratio $\langle S/N \rangle$ with azimuth angle θ. Plots are given for three incidence angles ι_o and four illumination scattering characteristics.

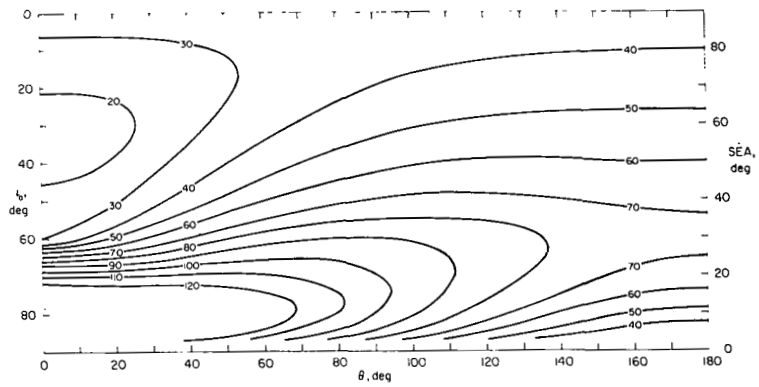

(a) Mars (Thorpe).

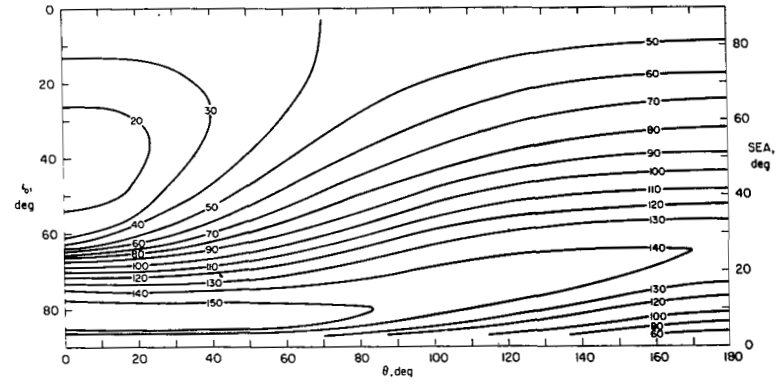

(c) Colorado basalt.

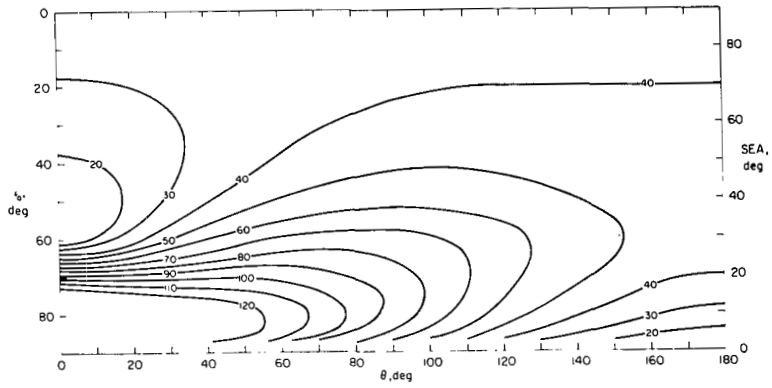

(b) Strong backscatter.

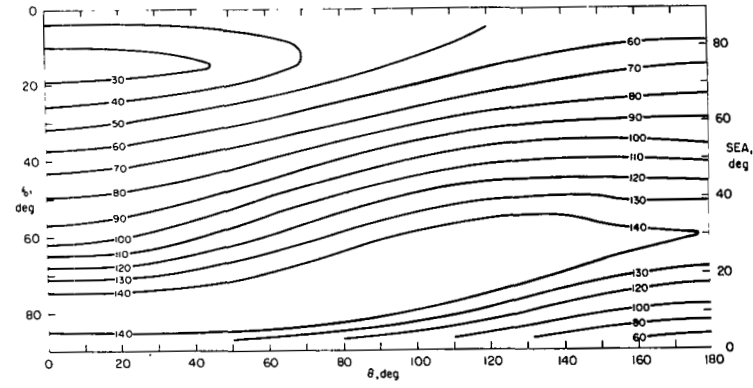

(d) Near Lambertian.

Figure 23.- Contour plots of cone signal-to-noise ratio $\langle S/N \rangle$ as a function of light incidence angle ι_o (or Sun elevation angle SEA) and azimuth angle θ for four illumination scattering characteristics. Emittance angle ϵ_o is 60^o (i.e., camera elevation angle of -30^o); cone slope α is 30^o; diameter c is 6 pixels; imaging condition is adequate, V/N = 100.

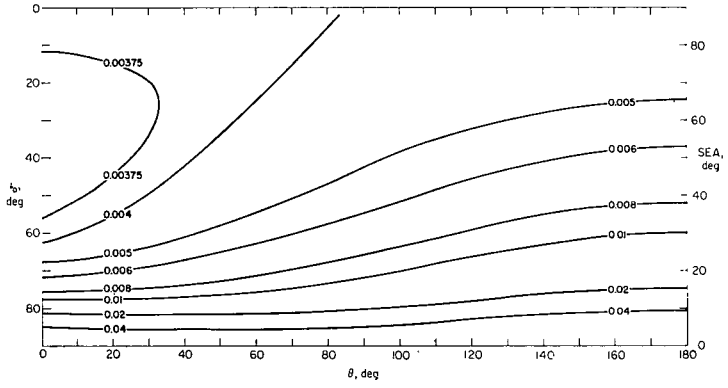

(a) Mars (Thorpe).

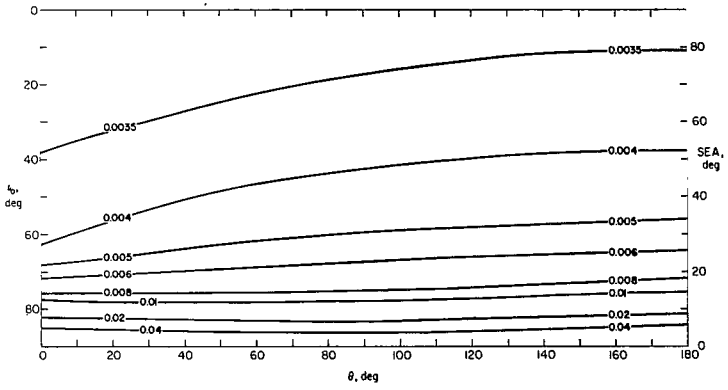

(c) Colorado basalt.

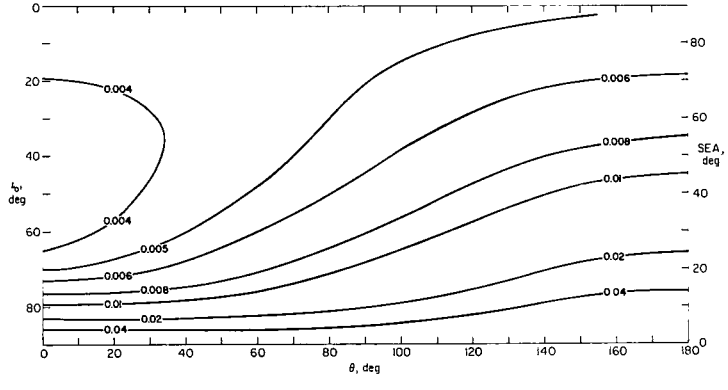

(b) Strong backscatter.

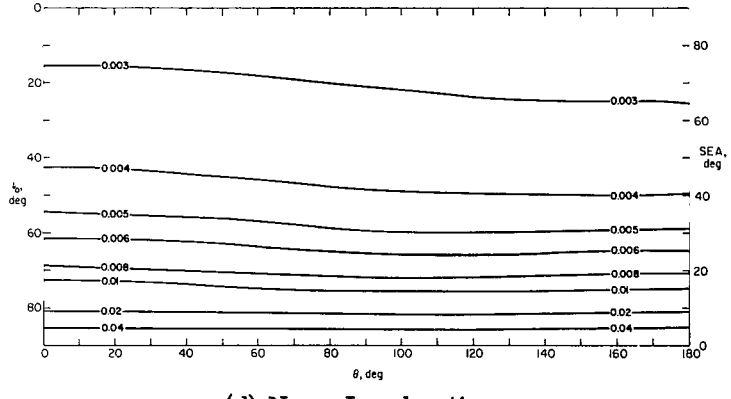

(d) Near Lambertian.

Figure 24.- Contour plots of minimum detectable albedo difference $\langle \Delta\rho \rangle$ as a function of light incidence angle ι_o (or Sun elevation angle SEA) and azimuth angle θ, for four illumination scattering characteristics. Emittance angle ϵ_o is 60^o (i.e., camera elevation angle of -30^o). Values are for a gain number of 4; twice these values represent a gain number of 5.

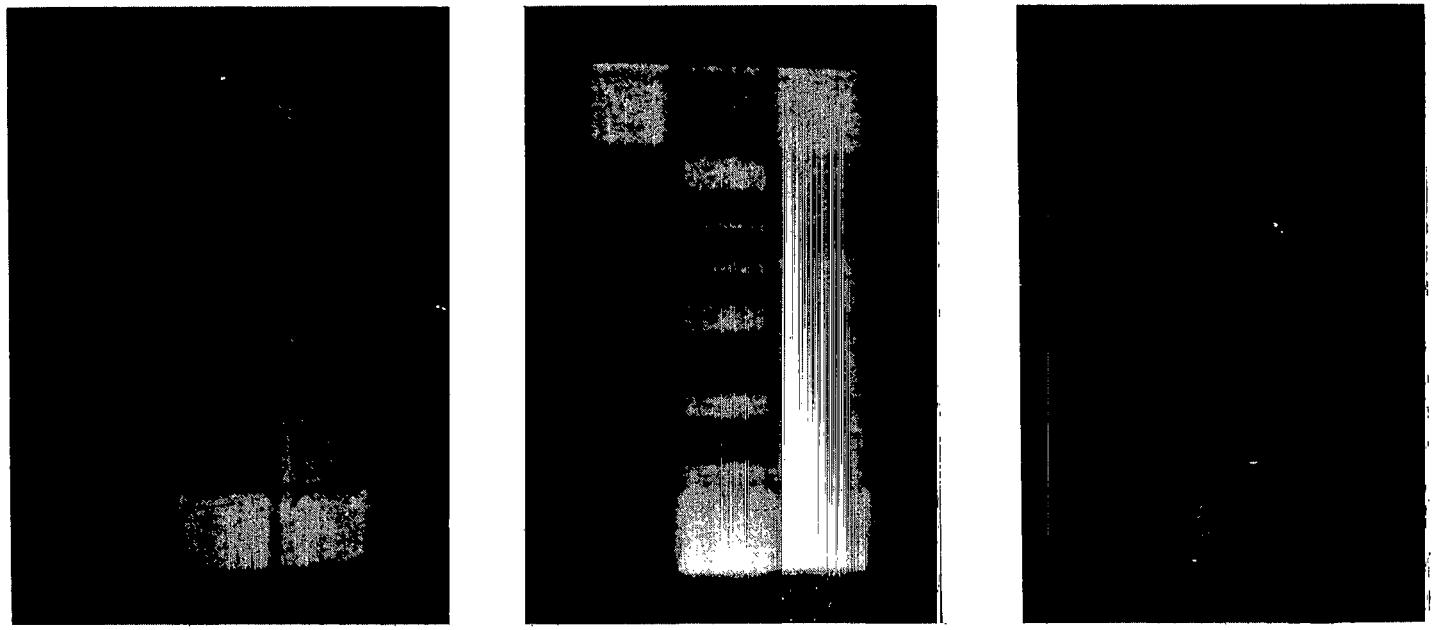

High resolution 1 High resolution 2 Survey

L-76-150

Figure 25.- Images of the reference test chart obtained with the two nearest-focused high-resolution diodes and the survey diode.

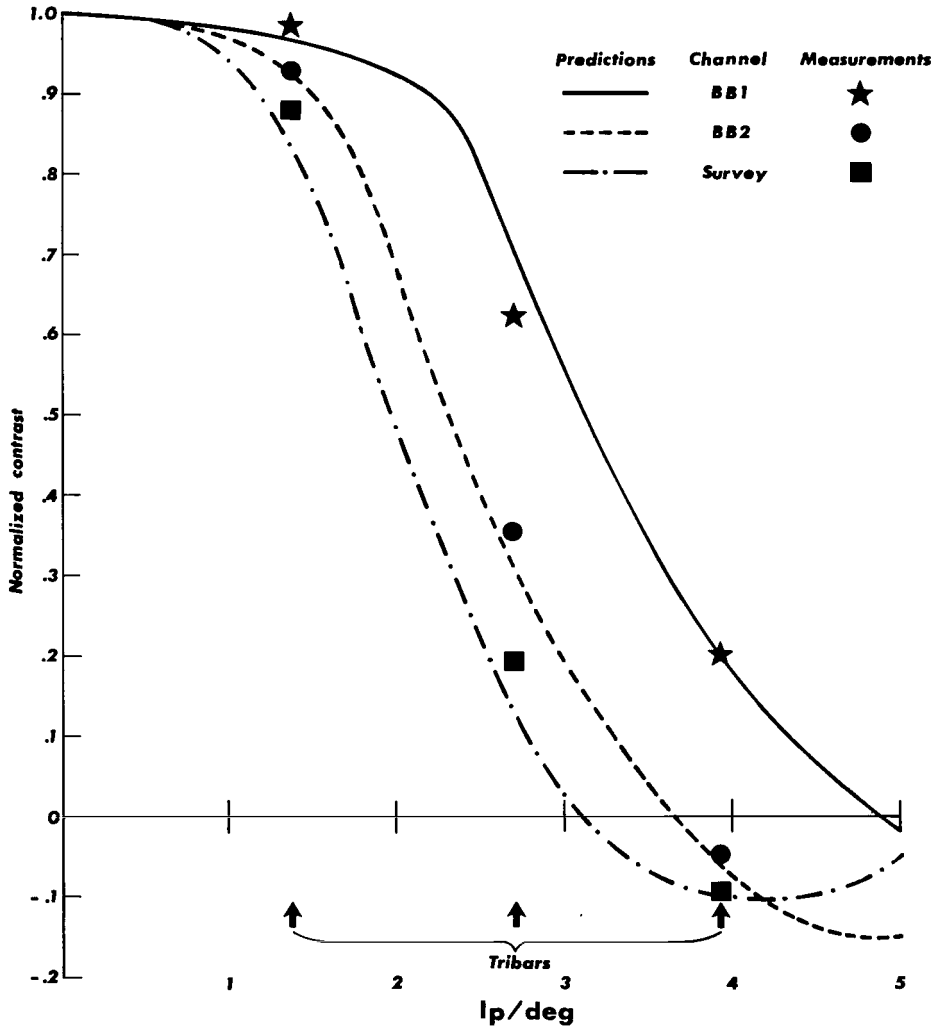

Figure 26.- Predicted square-wave frequency response of the camera for a target located 1.0 m away, and normalized tribar contrast measurements.

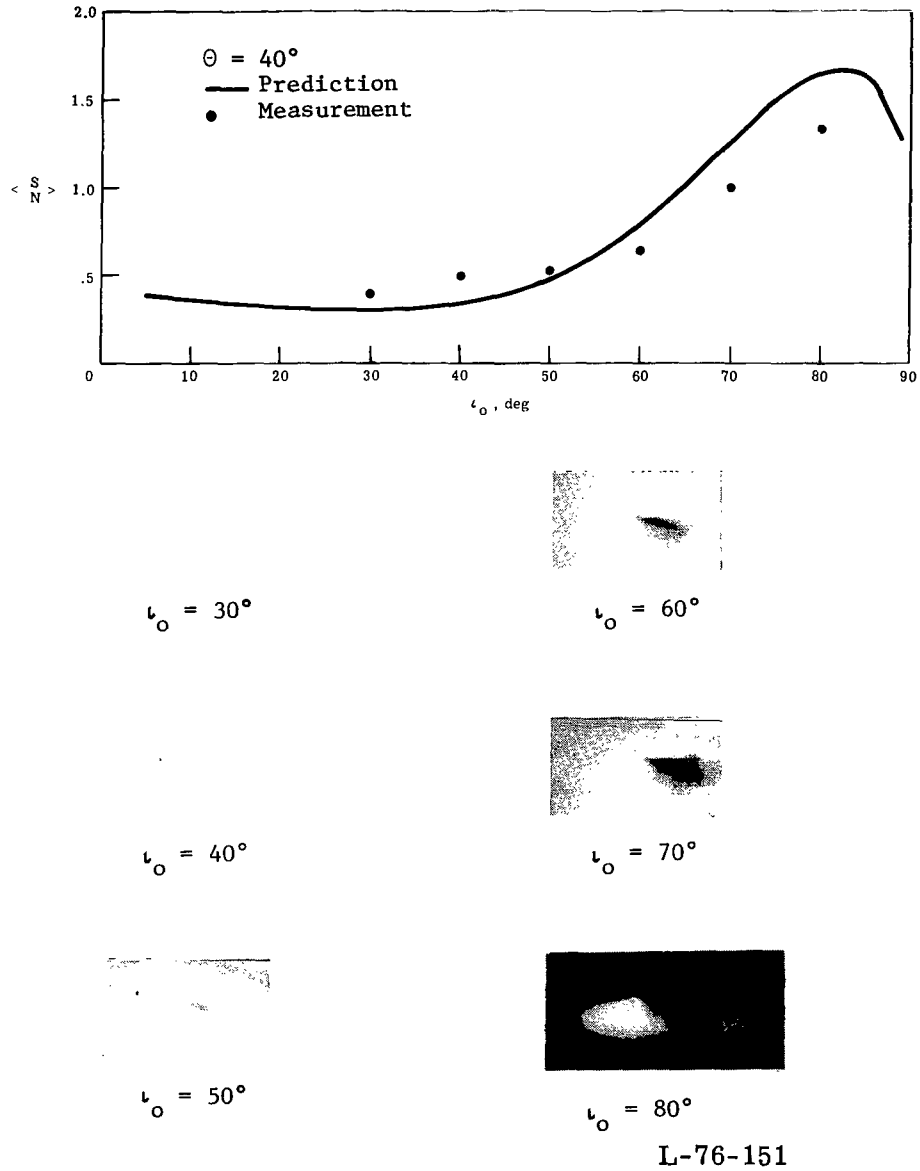

(a) $\theta = 40^{o}$.

Figure 27.- Cone images and their predicted and measured signal-to-noise ratios.

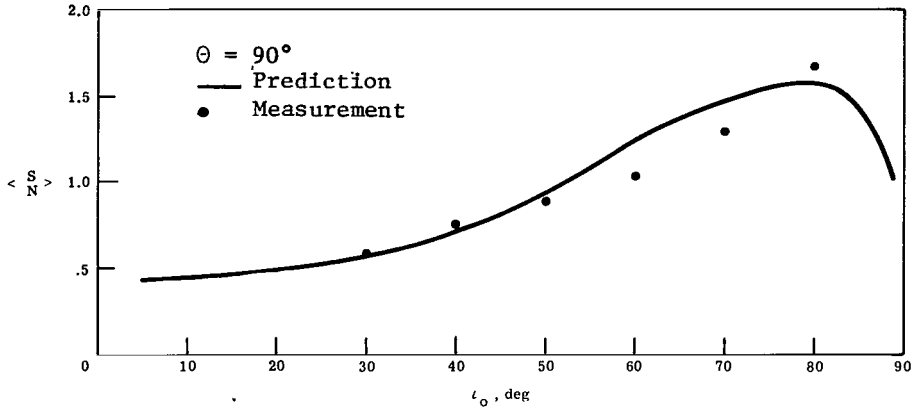

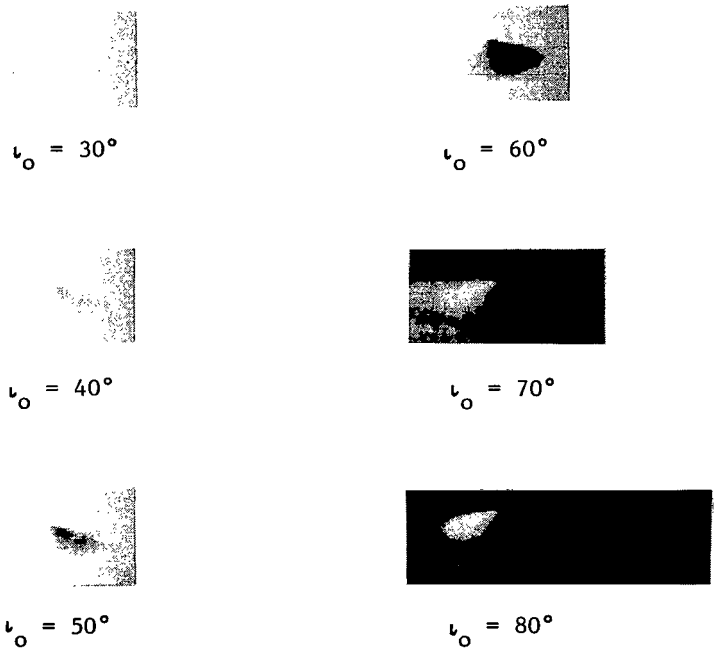

L-76-152

(b) $\theta = 90^{o}$.

Figure 27.- Continued.

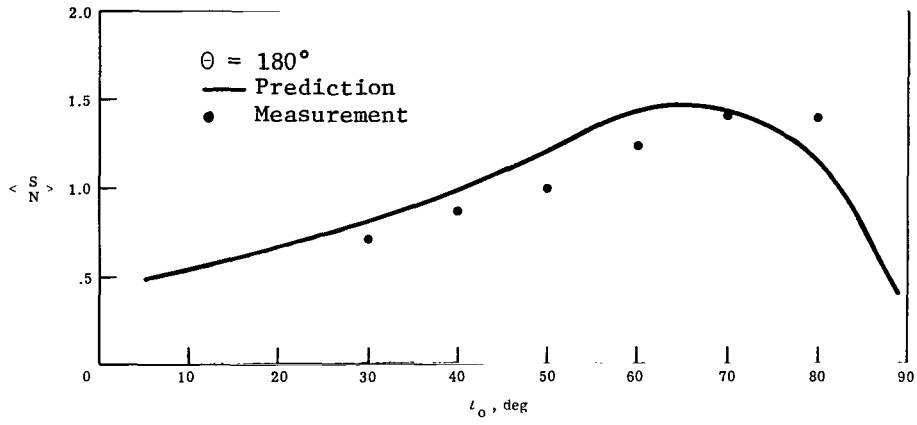

ι_o = 30°

ι_o = 60°

ι_o = 40°

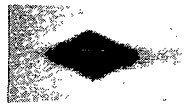

ι_o = 70°

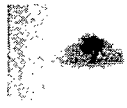

ι_o = 50°

ι_o = 80°

L-76-153

(c) $\theta = 180^o$.

Figure 27.- Concluded.